An analytical model for necking strains in stretched plates under dynamic biaxial loading

Nicolas Jacques

An analytical model for necking strains in stretched plates under dynamic biaxial loading

N. Jacques [a,*]

[a] *ENSTA Bretagne, UMR CNRS 6027, IRDL, 2 rue François Verny, F-29806 Brest cedex 9, France*

Abstract. A model for the prediction of localised necking in plates subjected to dynamic biaxial loading is presented. The proposed model extends the classic two-zone localisation analysis introduced by Marciniak and Kuczyński (1967) to include the contribution of inertia. Several examples of computations are presented to illustrate the influence of inertia, material rate-dependence and yield surface shape on plate necking under dynamic biaxial loading. It is found that inertia may significantly delay the occurrence of localised necking and increase the apparent ductility of the material. The results of the proposed model are compared to those of three-dimensional finite element simulations and a very good agreement is observed.

Keywords: Necking, Inertia, Two-zone model, Dynamic biaxial loading, Plastic flow localisation, Forming limits.

1. Introduction

The fracture of ductile materials is often preceded by the onset of plastic flow instabilities, such as shear banding or necking. This is an important issue for a number of industrial applications. For instance, the occurrence of localised necking often limits the deformation that can be achieved during sheet metal forming operations (Banabic, 2010). The development of theoretical models for the prediction of plastic flow localisation in thin metal sheets has received much attention in the literature. A seminal work was carried out by Hill (1952). He investigated the conditions for the occurrence of bifurcation into a localised deformation mode in an initially uniform rigid-plastic plate obeying the J_2 flow theory and deformed in its plane. He obtained closed-form expressions for the bifurcation strain and the

* Corresponding author. Tel.: +33 2 98 34 89 36; fax: +33 2 98 34 87 30.

E-mail address: nicolas.jacques@ensta-bretagne.fr (N. Jacques)

neck orientation. However, he found that a bifurcation is possible only if the ratio of the principal values of the in-plane strain tensor is negative (which was in contradiction with experimental observations). The bifurcation analysis of Hill (1952) was revisited by Stören and Rice (1975). They showed that a bifurcation is possible under biaxial stretching (i.e. when the principal strain ratio is positive) if the J_2 deformation theory is considered instead of the J_2 flow theory. Hutchinson and Neal (1978a) observed that a bifurcation can be predicted using the J_2 flow theory for positive values of the strain ratio when elasticity is taken into account. This shows that the prediction of plastic flow instabilities is very sensitive to details of the constitutive relation. Bifurcation analyses can be applied only to time-independent problems (only rate-independent solids and quasi-static deformations can be considered). However, it is known that strain-rate sensitivity may hinder the development of necks and increase the ductility, see for e.g. (Ghosh, 1977a-b; Hutchinson and Neale, 1977).

For viscoplastic materials, an alternative approach to analyse necking problems is the linear perturbation analysis (also named linear stability analysis). In this method, an infinitesimal perturbation is superimposed on a homogenous background solution. The growth rate of the perturbation can be either negative (indicating that the background plastic flow is stable) or positive. Using linear perturbation analysis, Hutchinson et al. (1978) obtained an exact solution for the early growth of plane strain necks. The linear stability analysis was applied for the first time to necking in viscoplastic sheets under biaxial loading by Dudzinski and Molinari (1988). See also (Dudzinski and Molinari, 1991; Toth et al., 1995; Boudeau and Gelin, 2000; Li et al., 2012) for other applications of the linear stability analysis to sheet necking.

Another approach to the prediction of necking during sheet forming operations was initiated by Marciniak and Kuczyński (1967), see also (Marciniak et al., 1973). The model developed by these authors assumed the existence of an initial imperfection in the sheet in the form of a band of reduced initial thickness. The deformation and stress fields inside and outside the band are supposed uniform and the evolution of the strain in these two regions is obtained by considering equilibrium. The loss of stability of the plastic flow manifests itself by a gradual concentration of the deformation in the imperfection and eventually by the full localisation of the plastic flow (corresponding to the occurrence of localised necking). The model proposed by Marciniak and Kuczyński (1967) assumes that the neck is perpendicular to the main straining direction and is therefore restricted to biaxial tension (positive values of the principal strain ratio). The two-zone approach was extended to the negative strain ratio range by

Hutchinson and Neale (1978a) by considering an arbitrary neck orientation. The two-zone model is commonly used in industry for the design of sheet forming processes and commercial computer programs based on this method are available (Banabic, 2010; Banabic et al., 2010). As mentioned previously, the prediction of plastic flow instabilities is very sensitive to the constitutive model assumed. For this reason, many works have been devoted to the implementation of complex constitutive relations in the two-zone model. Some examples of constitutive models that have been employed in forming limit analyses are anisotropic plasticity models (Parmar and Mellor, 1978; Ferron and Mliha Touati, 1985; Barlat, 1987; Lian et al., 1989; Kuroda and Tvergaard, 2000), kinematic hardening models (Tvergaard, 1980; Lu and Lee, 1987), viscoplastic models (Hutchinson and Neale, 1978b; Neale and Chater, 1981; Nie and Lee, 1981), ductile damage models (Needleman and Triantafyllidis, 1978; Chu and Needleman, 1980; Barlat et al., 1984).

The works discussed previously are dedicated to quasi-static loading conditions (inertia effects are neglected). Under dynamic loading, inertia can play a significant role in the development of plastic flow instabilities. For instance, inertia is known to be responsible for the occurrence of multiple necking. This behaviour has been observed in experiments on dynamic expansion of rings (Grady and Benson, 1983; Altinova et al., 1996; Zhang and Ravi-Chandar, 2006, 2008), tubes (Zhang and Ravi-Chandar, 2010) and hemispheres (Mercier et al., 2010). Dynamic expansion experiments have also revealed that a significant increase in ductility may take place under dynamic loading. Zhang and Ravi-Chandar (2008) observed that the evolution of the strain at the onset of localisation with loading rate is dependent on the size of the specimen. This suggests that inertia plays a key role in the enhancement of ductility under dynamic loading. The influence of inertia on plastic flow instabilities at high strain-rate has also been enlightened in several studies based on numerical simulations, see for e.g. (Han and Tvergaard, 1995; Hu and Daehn, 1996; Guduru and Freund, 2002; Xue et al., 2008; Rodríguez-Martínez et al., 2013b; Vaz-Romero et al., 2017). Enhancement of ductility at high loading rate has also been observed for more complex configurations. Balanethiram and Daehn (1994) and Balanethiram et al. (1994) showed that for several materials (interstitial free iron, 6061 aluminium and OFHC copper) a significant increase in formability can be achieved by using high speed forming processes, such as electro-hydraulic forming. Substantial improvements in formability under electro-hydraulic forming conditions are also reported in (Golovashchenko et al., 2013; Rohatgi et al., 2014). It is interesting to notice that

inertia may also affect the development of plastic instabilities at microscale, such as void coalescence in porous solids (Jacques et al., 2012; Molinari et al., 2015).

As mentioned previously, the main theoretical approaches for the prediction of necking are concerned by quasi-static conditions (inertia is disregarded). The modelling of plastic instabilities under dynamic loading has received less attention. Most of the contributions rely on linear perturbation methods. Fressengeas and Molinari (1994) extended the plane-strain linear stability analysis of Hutchinson et al. (1978) to include inertia effects. They showed that inertia hinders the growth of long-wavelength modes, while stress triaxiality effects impede the development of short-wavelength modes. The competition between inertia and stress triaxiality effects leads to the emergence of a characteristic neck spacing. In other words, the linear perturbation analysis is able to explain the occurrence of multiple necking under dynamic loading. Using a different formalism, Shenoy and Freund (1999) also proposed a linear stability analysis to describe dynamic instabilities under plane strain conditions. The case of cylindrical bars under uniaxial tension has been considered by Mercier and Molinari (2003), Zhou et al. (2006) and El Maï et al. (2014). Recently, Jouve (2010, 2015) and Zaera et al. (2015) developed linear perturbation analyses to study the development of necking in plates subjected to dynamic biaxial loading. In (Zaera et al., 2015), the predictions of the linear stability analysis are compared to the results of dynamic finite element computations of plate necking. It appears that the linear stability analysis accurately captures the characteristic neck spacing and orientation.

To the author's knowledge, the only attempt to incorporate inertia in the two-zone approach was made by Xue et al. (2008). The one-dimensional model proposed by these authors is able to capture the combined role of strain-rate sensitivity, inertia and loading rate on neck retardation, but is restricted to plane strain conditions.

The present work deals with the development of a model to predict the occurrence of localised necking and the corresponding limit strains in ductile plates subjected to dynamic biaxial loading. More precisely, the goal is to generalise the two-zone approach developed by Marciniak and Kuczyński (1967) and Hutchinson and Neale (1978a) to include the effects of material inertia. The paper is organised as follows. The proposed model is presented in Section 2. The governing equations, the kinematic assumptions and the method employed to include inertia effects (based on the virtual work principle) are described. Results obtained with the model are presented in Section 3. They illustrate the influence of inertia, material strain-rate dependence and yield surface shape on plastic flow localisation under dynamic

biaxial loading. Moreover, to assess the predictive capabilities of the proposed model, comparisons with results of finite element simulations are presented. The conclusions of the present study are given in Section 4.

2. Analytical model for dynamic neck development

2.1 Problem description and kinematic assumptions

A thin metal sheet subjected to in-plane biaxial stretching is considered. A Lagrangian frame (X_1, X_2, X_3) associated to the principal straining directions is introduced, with X_3 being normal to the plate. In this frame, the overall deformation gradient applied to the sheet can be expressed as

$$\boldsymbol{F} = \begin{bmatrix} F_{11} & 0 & 0 \\ 0 & F_{22} & 0 \\ 0 & 0 & F_{33} \end{bmatrix}_{(X_1,X_2,X_3)} \tag{1}$$

The stretch rate in the main loading directions is assumed to be constant,

$$F_{11} = 1 + \dot{F}_{11} \cdot t \qquad \text{and} \qquad F_{22} = 1 + \dot{F}_{22} \cdot t \tag{2}$$

It is considered that $\dot{F}_{22} > 0$ and $\dot{F}_{11} = \chi \cdot \dot{F}_{22}$ with $0.5 \leq \chi \leq 1$. Assuming that the material is incompressible F_{33} can be expressed as a function of the in-plane components:

$$F_{33} = \frac{1}{F_{11} \cdot F_{22}} \tag{3}$$

It is assumed that the mode of localisation that will occur during the sheet deformation is a regular multiple necking pattern. The spacing between necks (measured in the undeformed configuration) is denoted by L_0 and the orientation of the necks is defined by the angle ψ shown in Fig. 1-a. A Lagrangian frame (X_α, X_β, X_3) associated with the neck orientation is introduced (X_α being in the neck direction). The expression of the overall deformation gradient in this frame is given by

$$\boldsymbol{F} = \begin{bmatrix} F_{11}.\cos^2\psi + F_{22}.\sin^2\psi & (F_{22} - F_{11}).\sin\psi.\cos\psi & 0 \\ (F_{22} - F_{11}).\sin\psi.\cos\psi & F_{11}.\sin^2\psi + F_{22}.\cos^2\psi & 0 \\ 0 & 0 & F_{33} \end{bmatrix}_{(X_\alpha,X_\beta,X_3)} \tag{4}$$

(a)

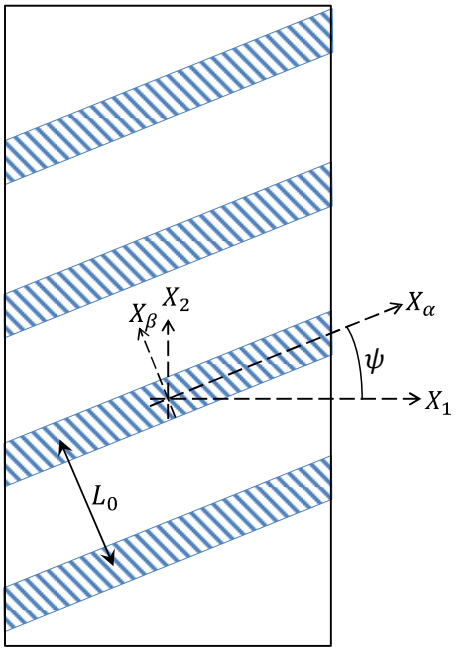

(b)

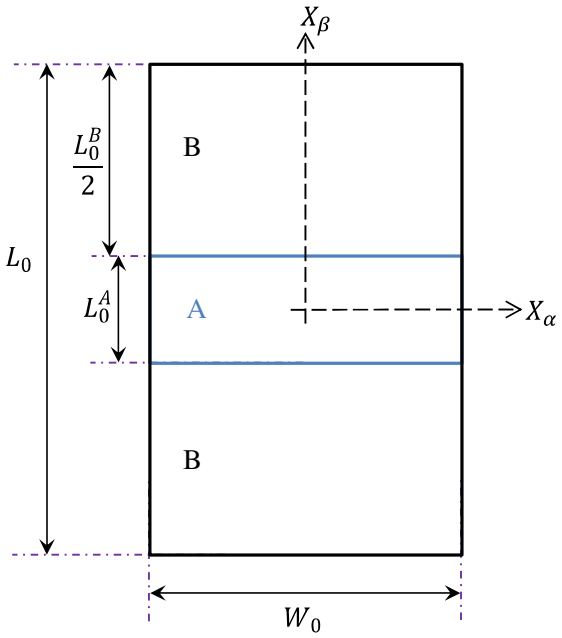

Fig. 1. Illustration of the two-zone model. (a) Definition of geometric quantities and the frames associated to the loading and the necks. (b) Initial geometry of the unit-cell considered for the derivation of the model.

To describe the occurrence and growth of necks during the sheet deformation, a two-zone approach is adopted. For the development of the model, a unit-cell is considered. Its initial

geometry is displayed in Fig. 1-b. The initial length of the cell is taken as the inter-neck distance L_0 and its initial width is denoted by W_0. The unit-cell is composed of two regions, A and B. The initial thicknesses of these two zones are assumed to be uniform and are denoted by h_0^A and h_0^B, with $h_0^A < h_0^B$. Zone A will also be named the imperfection in the following.

It is assumed that the deformation is uniform in the two zones. Therefore, the in-plane displacement field in zone A can be written in the following form

$$U_\alpha^A = (F_{\alpha\alpha}^A - 1).X_\alpha + F_{\alpha\beta}^A.X_\beta \tag{5a}$$

$$U_\beta^A = F_{\beta\alpha}^A.X_\alpha + \left(F_{\beta\beta}^A - 1\right).X_\beta \tag{5b}$$

and the displacement field in zone B is given by

$$U_\alpha^B = (F_{\alpha\alpha}^B - 1).X_\alpha + \mathrm{sgn}\left(X_\beta\right).\left[F_{\alpha\beta}^A.\frac{L_0^A}{2} + F_{\alpha\beta}^B.\left(\left|X_\beta\right| - \frac{L_0^A}{2}\right)\right] \tag{6a}$$

$$U_\beta^B = F_{\beta\alpha}^B.X_\alpha + \mathrm{sgn}\left(X_\beta\right).\left[\left(F_{\beta\beta}^A - 1\right).\frac{L_0^A}{2} + \left(F_{\beta\beta}^B - 1\right).\left(\left|X_\beta\right| - \frac{L_0^A}{2}\right)\right] \tag{6b}$$

$\boldsymbol{F}^A$ and $\boldsymbol{F}^B$ correspond to the deformation gradient in zone A and B, respectively, and sgn() denotes the signum function. The continuity of the displacement at the interface between the two zones requires that

$$F_{\alpha\alpha}^A = F_{\alpha\alpha}^B = F_{\alpha\alpha} \tag{7a}$$

$$F_{\beta\alpha}^A = F_{\beta\alpha}^B = F_{\beta\alpha}. \tag{7b}$$

The other components of the deformation gradients in zones A and B are linked to the overall deformation gradient by the following relationships

$$R.F_{\beta\beta}^A + (1 - R).F_{\beta\beta}^B = F_{\beta\beta} \tag{8a}$$

$$R.F_{\alpha\beta}^A + (1 - R).F_{\alpha\beta}^B = F_{\alpha\beta} \tag{8b}$$

where $R = L_0^A/L_0$. From Eqs. (7-8), it appears that the present model involves only two independent kinematic unknowns.

As the stretch rate in the main loading directions is assumed to be constant, the in-plane components of the overall acceleration gradient are equal to zero, $\ddot{F}_{\alpha\alpha} = \ddot{F}_{\beta\beta} = \ddot{F}_{\beta\alpha} = \ddot{F}_{\alpha\beta} = 0$ (see Eqs. (2) and (4)). Hence, from Eqs. (5-6), the in-plane acceleration field can be written in the following form:

$$\ddot{U}_\alpha^A = \ddot{F}_{\alpha\beta}^A.X_\beta \tag{9a}$$

$$\ddot{U}_{\beta}^{A} = \ddot{F}_{\beta\beta}^{A}.X_{\beta} \tag{9b}$$

$$\ddot{U}_{\alpha}^{B} = \mathrm{sgn}(X_{\beta}).\left[\ddot{F}_{\alpha\beta}^{A}.\frac{L_0^A}{2} + \ddot{F}_{\alpha\beta}^{B}.\left(|X_{\beta}| - \frac{L_0^A}{2}\right)\right] \tag{9c}$$

$$\ddot{U}_{\beta}^{B} = \mathrm{sgn}(X_{\beta}).\left[\ddot{F}_{\beta\beta}^{A}.\frac{L_0^A}{2} + \ddot{F}_{\beta\beta}^{B}.\left(|X_{\beta}| - \frac{L_0^A}{2}\right)\right] \tag{9d}$$

with the following relations between the components of the acceleration gradients in zones A and B

$$R.\ddot{F}_{\beta\beta}^{A} + (1-R).\ddot{F}_{\beta\beta}^{B} = 0 \tag{10a}$$

$$R.\ddot{F}_{\alpha\beta}^{A} + (1-R).\ddot{F}_{\alpha\beta}^{B} = 0 \tag{10b}$$

The out-of-plane components of the acceleration, $\ddot{U}_3^B$ and $\ddot{U}_3^A$, are neglected in the present model. For thin plates, these components are expected to be negligible as compared to the in-plane components.

2.2 Virtual work principle

As mentioned in the previous section, the two-zone model involves two independent kinematic unknowns. It is therefore necessary to obtain two equations that describe the evolution of these variables. In the standard two-zone model (in which inertia effects are neglected), homogeneous deformation and stress fields are assumed inside and outside the imperfection and therefore equilibrium is automatically satisfied in these two regions. The neck development is determined by considering the continuity of the force components at the interface between the two zones. This approach cannot be applied when inertia is taken into account. Indeed, the balance of momentum equation cannot be fulfilled at any point of the cell. This difficulty has been overcome by employing the virtual work principle (i.e. the weak form of the balance of momentum equation). The application of the virtual work principle, together with the simplified kinematics associated to the two-zone model, will give two ordinary differential equations for the evolution of the deformation in zone A. These equations include a term related to inertia.

Considering the kinematic assumptions introduced in the previous section, Eqs. (5-8), a virtual variation of the displacement field can be written in the following form:

zone A: $\delta U_{\alpha}^{A} = \delta F_{\alpha\beta}^{A}.X_{\beta}$ (11a)

$$\delta U_\beta^A = \delta F_{\beta\beta}^A . X_\beta \tag{11b}$$

zone B: $$\delta U_\alpha^B = \mathrm{sgn}(X_\beta).\left[\delta F_{\alpha\beta}^A.\frac{L_0^A}{2} + \delta F_{\alpha\beta}^B.\left(|X_\beta| - \frac{L_0^A}{2}\right)\right] \tag{11c}$$

$$\delta U_\beta^B = \mathrm{sgn}(X_\beta).\left[\delta F_{\beta\beta}^A.\frac{L_0^A}{2} + \delta F_{\beta\beta}^B.\left(|X_\beta| - \frac{L_0^A}{2}\right)\right] \tag{11d}$$

where $\delta F_{\alpha\beta}^A$, $\delta F_{\beta\beta}^A$, $\delta F_{\alpha\beta}^B$ and $\delta F_{\beta\beta}^B$ are virtual variations of the components of the deformation gradients in zones A and B. From Eqs. (8a-b), we also have the following relations

$$R.\delta F_{\beta\beta}^A + (1-R).\delta F_{\beta\beta}^B = 0 \tag{12a}$$

$$R.\delta F_{\alpha\beta}^A + (1-R).\delta F_{\alpha\beta}^B = 0 \tag{12b}$$

The virtual work principle for the unit-cell can be written as

$$\delta W_{int} + \delta W_{kin} = \delta W_{ext} \tag{13}$$

where δW_{int} is the virtual work of internal forces, δW_{kin} the virtual work of inertia forces and δW_{ext} the virtual work of external forces. In the present case, as no body force is applied to the sheet and as kinematic boundary conditions are considered, the virtual work of external forces is equal to zero, $\delta W^{ext} = 0$. As stated previously, the deformation gradient and the stress are supposed uniform in zones A and B. Moreover, plane stress conditions are assumed. Thus, the virtual work of internal forces can be expressed as

$$\delta W_{int} = h_0^A L_0^A W_0\left(P_{\beta\alpha}^A \delta F_{\alpha\beta}^A + P_{\beta\beta}^A \delta F_{\beta\beta}^A\right) + h_0^B L_0^B W_0\left(P_{\beta\alpha}^B \delta F_{\alpha\beta}^B + P_{\beta\beta}^B \delta F_{\beta\beta}^B\right) \tag{14}$$

where $\boldsymbol{P}^A$ and $\boldsymbol{P}^B$ denote the nominal stress tensor in zones A and B, respectively. Considering Eqs. (12a-b), this expression can be rewritten in the following form

$$\delta W_{int} = W_0 L_0 R\left(\left(h_0^A P_{\beta\alpha}^A - h_0^B P_{\beta\alpha}^B\right)\delta F_{\alpha\beta}^A + \left(h_0^A P_{\beta\beta}^A - h_0^B P_{\beta\beta}^B\right)\delta F_{\beta\beta}^A\right) \tag{15}$$

The virtual work of inertial forces is given by

. $$\delta W_{kin} = \delta W_{kin}^A + \delta W_{kin}^B \quad \text{with} \tag{16}$$

$$\delta W_{kin}^A = 2\rho_0 h_0^A \int_0^{L_0^A/2}\int_{-W_0/2}^{W_0/2}\left(\ddot{U}_\alpha^A \delta U_\alpha^A + \ddot{U}_\beta^A \delta U_\beta^A\right)\mathrm{d}X_\alpha \mathrm{d}X_\beta \quad \text{and}$$

$$\delta W_{kin}^B = 2\rho_0 h_0^B \int_{L_0^A/2}^{L_0/2}\int_{-W_0/2}^{W_0/2}\left(\ddot{U}_\alpha^B \delta U_\alpha^B + \ddot{U}_\beta^B \delta U_\beta^B\right)\mathrm{d}X_\alpha \mathrm{d}X_\beta$$

where δW_{kin}^A and δW_{kin}^B correspond respectively to the contributions of zone A and zone B.

From Eqs. (9a-b) and (11a-b), it can be shown that

$$\ddot{U}_\alpha^A \delta U_\alpha^A + \ddot{U}_\beta^A \delta U_\beta^A = X_\beta^2 \left(\ddot{F}_{\alpha\beta}^A \delta F_{\alpha\beta}^A + \ddot{F}_{\beta\beta}^A \delta F_{\beta\beta}^A \right) \tag{17}$$

After integration, the following expression of the contribution of zone A to the virtual inertial work is obtained

$$\delta W_{kin}^A = \frac{\rho_0 h_0^A W_0 {L_0^A}^3}{12} \left(\ddot{F}_{\alpha\beta}^A \delta F_{\alpha\beta}^A + \ddot{F}_{\beta\beta}^A \delta F_{\beta\beta}^A \right) \tag{18}$$

The acceleration and the virtual displacement in zone B are given by Eqs. (9c-d) and Eqs. (11c-d), respectively. Considering also Eqs. (10a-b) and (12a-b), it can be shown that

$$\ddot{U}_\alpha^B \delta U_\alpha^B + \ddot{U}_\beta^B \delta U_\beta^B = \left(\frac{L_0^A}{2} - \frac{R}{1-R} \left(\left| X_\beta \right| - \frac{L_0^A}{2} \right) \right)^2 . \left(\ddot{F}_{\alpha\beta}^A \delta F_{\alpha\beta}^A + \ddot{F}_{\beta\beta}^A \delta F_{\beta\beta}^A \right) \tag{19}$$

After integration, one obtains

$$\delta W_{kin}^B = \frac{\rho_0 h_0^B W_0 L_0^3 R^2 (1-R)}{12} \left(\ddot{F}_{\alpha\beta}^A \delta F_{\alpha\beta}^A + \ddot{F}_{\beta\beta}^A \delta F_{\beta\beta}^A \right) \tag{20}$$

From Eqs. (18) and (20), the virtual inertial work for the unit-cell (zone A + zone B) can be written in the following form

$$\delta W_{kin} = \frac{\rho_0 W_0 L_0^3}{12} (R^3 h_0^A + R^2 (1-R) h_0^B) \left(\ddot{F}_{\alpha\beta}^A \delta F_{\alpha\beta}^A + \ddot{F}_{\beta\beta}^A \delta F_{\beta\beta}^A \right) \tag{21}$$

The virtual work equation for the unit-cell (13) should be satisfied for any virtual variation of the deformation gradient. Therefore, the following ordinary differential equations are obtained:

$$\ddot{F}_{\alpha\beta}^A = \frac{h_0^B P_{\beta\alpha}^B - h_0^A P_{\beta\alpha}^A}{C_d} \tag{22a}$$

$$\ddot{F}_{\beta\beta}^A = \frac{h_0^B P_{\beta\beta}^B - h_0^A P_{\beta\beta}^A}{C_d} \tag{22b}$$

with $C_d = \frac{\rho_0 L_0^2}{12} (R^2 h_0^A + R(1-R) h_0^B)$.

C_d is a coefficient that characterises inertia effects. It depends on the mass density of the material ρ_0, the initial thicknesses of the two zones h_0^A and h_0^B, the initial unit-cell length L_0 (that corresponds to the distance between necks) and the ratio R of the initial imperfection length to the initial unit-cell length.

2.3 Constitutive equations

As a Lagrangian framework has been used for the derivation of the dynamic two-zone model, Eqs (22a-b) involve the components of the nominal stress tensor. However, common plasticity models for metals are formulated using the Cauchy stress tensor $\boldsymbol{\sigma}$. The components of the nominal and Cauchy stress tensors are related by the following relationship

$$P_{ij}^X = \det(\boldsymbol{F}^X) \cdot (F_{ik}^X)^{-1} \cdot \sigma_{kj}^X \tag{23}$$

with $X = A$ or $X = B$. For an incompressible solid, $\det(\boldsymbol{F}^X) = 1$. A rigid-plastic behaviour is assumed (elastic strains are neglected). In this case, it is convenient to employ constitutive relations based on a strain-rate potential (Hill, 1987) as they provide an explicit expression of the stress,

$$s_{ij}^X = \bar{\sigma}^X . \frac{\partial \varphi\left(D_{ij}^X\right)}{\partial D_{ij}^X} \tag{24}$$

where s_{ij}^X is the deviatoric stress tensor and D_{ij}^X is the strain-rate tensor

$$D_{ij}^X = \frac{1}{2}\left(L_{ij}^X + L_{ji}^X\right) \qquad \text{with} \qquad L_{ij}^X = \dot{F}_{ik}^X . \left(F_{kj}^X\right)^{-1} \tag{25}$$

φ is the strain-rate potential and $\bar{\sigma}^X$ is a positive scalar number. Generally, $\bar{\sigma}^X$ is taken as the flow stress in uniaxial tension. $\bar{\sigma}^X$ may be strain, strain-rate and temperature dependent, $\bar{\sigma}^X = \bar{\sigma}(\bar{\varepsilon}^X, \dot{\bar{\varepsilon}}^X, T^X)$. The evolution of the effective plastic strain $\bar{\varepsilon}^X = \int_0^t \dot{\bar{\varepsilon}}^X . \mathrm{d}\tau$ and the temperature T^X (assuming adiabatic conditions) in the two zones is given by

$$\dot{\bar{\varepsilon}}^X = \varphi\left(D_{ij}^X\right) \qquad \text{and} \qquad \dot{T}^X = \frac{\beta_{TQ}}{\rho_0 C_0} \bar{\sigma}^X \dot{\bar{\varepsilon}}^X \tag{26}$$

where C_0 is the heat capacity of the material and β_{TQ} the Taylor-Quiney coefficient (fraction of plastic work converted to heat).

In the present study, two different strain-rate potentials will be employed. The first corresponds to the classic J_2 flow theory:

$$\varphi\left(D_{ij}\right) = \sqrt{\frac{2}{3} D_{ij} D_{ij}} \tag{27}$$

In this case, the deviatoric stress is given by

$$s_{ij}^X = \frac{2\bar{\sigma}^X}{3\dot{\bar{\varepsilon}}^X} D_{ij}^X$$

The second strain-rate potential considered was proposed by Cazacu and Revil-Baudard (2017). It accounts for the influence of the third invariant of the strain-rate tensor:

$$\varphi(D_{ij}) = \frac{\sqrt{j_2}}{B}\left(1 + \beta\frac{j_3^2}{j_2^3}\right) \tag{28}$$

$$\text{with} \quad j_2 = \frac{1}{2}D_{ij}D_{ij} \qquad j_3 = \det(\boldsymbol{D}) \qquad B = \frac{1+4\beta/27}{\sqrt{4/3}}$$

where β is a parameter of the model that describes the influence of the third invariant of the strain-rate tensor.

For an incompressible material, the constitutive relation only provides the deviatoric stress. Using the plane stress condition, $\sigma_{33}^X = 0$, the following expression of the Cauchy stress tensor is obtained

$$\sigma_{ij}^X = s_{ij}^X - s_{33}^X\delta_{ij} \tag{29}$$

with δ_{ij} being the Kronecker delta.

2.4 Bridgman correction factor

The two-zone model is based on simplified kinematic assumptions. The deformation is assumed uniform in the two zones and therefore the stress is homogenous through the sheet thickness. However, the development of necking leads to a triaxial stress field and stress gradients in the neck region. In order to account for triaxiality effects, the Bridgman (1952) correction factor is introduced in the modelling. To our knowledge, the idea of using 1D or 2D models enhanced with the Bridgman correction factor to analyse multiple necking under dynamic loading was proposed by Walsh (1984). Subsequently, this methodology has been employed in several studies and was found to be effective and accurate, see for e.g. (Fressengeas and Molinari, 1984; Zhou et al., 2006; Vadillo et al., 2012; Rodríguez-Martínez et al., 2013a, 2013b; Zaera et al., 2015; Vaz-Romero et al., 2017).

Let us denote the Eulerian coordinate in the direction perpendicular to the sheet mid-plane by x_3. In the Bridgman (1952) analysis, the stress distribution across the neck σ_{ij}^{neck} is assumed to be the sum of a "uniform" stress σ_{ij}^A and a hydrostatic component σ_h varying with the x_3 coordinate:

$$\sigma_{ij}^{neck}(x_3) = \sigma_{ij}^A + \sigma_h(x_3).\delta_{ij} \tag{30}$$

The uniform stress σ_{ij}^{A} is obtained by assuming a uniform deformation field in the neck region and plane-stress conditions. In the present case, it corresponds to the stress given by the constitutive equations presented in section 2.3.

Bridgman (1952) obtained the following expression of the average stress $\hat{\sigma}_{\beta'\beta'}^{A}$ across the sheet thickness in the in-plane direction perpendicular to the neck (in the deformed configuration) $x_{\beta'}$:

$$\hat{\sigma}_{\beta'\beta'}^{A} = \frac{1}{2a}\int_{-a}^{a} \sigma_{\beta'\beta'}^{neck}(x_3).\,\mathrm{d}x_3 = B_1(\phi).\,\sigma_{\beta'\beta'}^{A} \tag{31}$$

where a is the sheet half-thickness at the centre of the neck and $B_1(\phi)$ is the Bridgman correction factor, given by[1]

$$B_1(\phi) = \sqrt{1+\frac{1}{\phi}}\cdot \ln\left(1+2\phi+2\sqrt{\phi(1+\phi)}\right) - 1 \qquad \text{with} \quad \phi = \frac{a}{2R_c} \tag{32}$$

where R_c is the maximum radius of curvature of the neck profile. The Bridgman correction factor describes the enhancement of the axial stress due to necking.

The Bridgman correction factor depends on the maximum radius of curvature of the neck profile. However, the two-zone model does not provide the complete geometry of the neck but only the maximum thickness reduction. To obtain an estimate of the argument of the Bridgman factor, it is considered that the imperfection region (zone A) in the two-zone model corresponds to the region where the curvature of the neck profile is positive. Moreover, it is assumed that the thickness variation is sinusoidal in this region (Fig. 2),

$$h(x_{\beta'}) = h^A + \frac{h^B - h^A}{2}\left(1-\cos\left(\frac{\pi.x_{\beta'}}{L^A}\right)\right), \tag{33}$$

where $x_{\beta'}$ is the Eulerian coordinate in the direction perpendicular to the neck; the neck centre is at $x_{\beta'} = 0$. With these assumptions, the half-sheet thickness at the neck centre and the maximum radius of curvature of the neck profile are equal to

$$a = \frac{h^A}{2} \qquad \text{and} \qquad R_c = \frac{2}{h''(0)} = \left(\frac{L^A}{\pi}\right)^2 \frac{4}{h^B - h^A} \tag{34}$$

Hence, the argument of the Bridgman correction factor can be expressed as

[1] It should be noticed that this expression was obtained by Bridgman (1952) assuming plane strain conditions. However, the validity of this formula for biaxial loadings has been assessed by Zaera et al. (2015) with the use of finite element computations.

$$\phi = \frac{\pi^2 h^A (h^B - h^A)}{16 (L^A)^2} \tag{35}$$

In this expression, h^A and h^B correspond respectively to the thickness of zone A and of zone B, and L^A to the length of zone A in the deformed configuration. These quantities can be computed using the following relationships

$$h^A = F_{33}^A h_0^A \qquad h^B = F_{33}^B h_0^B \qquad L^A = L_0^A \sqrt{{F_{\alpha\beta}^A}^2 + {F_{\beta\beta}^A}^2} \tag{36}$$

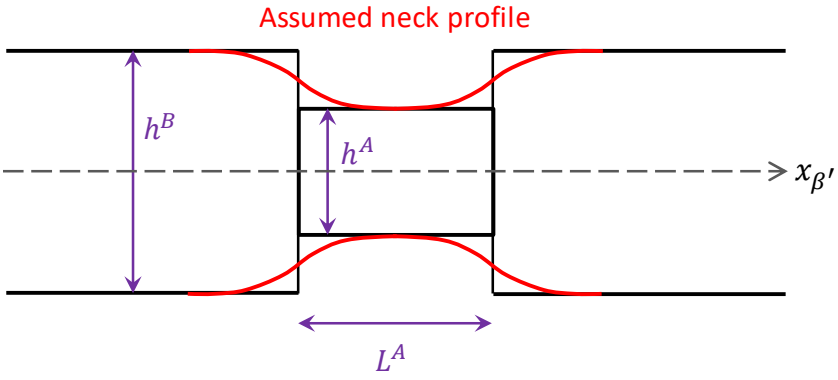

Fig. 2. Illustration of the neck profile used to estimate the argument of the Bridgman correction factor.

The component $P_{\beta\beta}^A$ of the nominal stress tensor is related to $\sigma_{\beta'\beta'}^A$ by the following relation (Malvern, 1959)

$$P_{\beta\beta}^A = \sigma_{\beta'\beta'}^A \frac{dS}{dS_0} \tag{37}$$

where dS_0 is the area of an infinitesimal surface of unit normal X_β in the undeformed configuration and dS the area of the corresponding deformed surface. Since $P_{\beta\beta}^A$ and $\sigma_{\beta'\beta'}^A$ are proportional, the Bridgman correction factor can be applied to the component $P_{\beta\beta}^A$ of the nominal stress tensor:

$$\hat{P}_{\beta\beta}^A = B_1(\phi).P_{\beta\beta}^A \tag{38}$$

To account for the stress enhancement due to necking in the present model, the "uniform" stress $P_{\beta\beta}^A$ is replaced by the average stress $\hat{P}_{\beta\beta}^A$ in Eq. (22b), leading to:

$$\ddot{F}_{\beta\beta}^A = \frac{h_0^B P_{\beta\beta}^B - h_0^A B_1(\phi) P_{\beta\beta}^A}{c_d} \tag{39}$$

2.5 Determination of the critical neck spacing and orientation

First, to illustrate how the model works, an example of computation is presented in Fig. 3. This figure shows the evolution of the maximum principal logarithmic strain inside (zone A) and outside the imperfection (zone B) (obtained by numerical integration of Eqs (22a) and (39), see appendix A for more details about the numerical implementation of the two-zone model) as a function of the overall maximum principal logarithmic strain. The material has a mass density of 7800 $\mathrm{kg/m^3}$ and an isotropic rate-independent rigid-plastic behaviour obeying the J_2 flow theory. Hardening is described by a power law relation

$$\bar{\sigma} = \sigma_0(\bar{\varepsilon})^n \tag{40}$$

with $n = 0.1$ and $\sigma_0 = 500\,MPa$. The loading conditions are $\dot{F}_{22} = 5000\,s^{-1}$ and $\dot{F}_{11} = 0$ (plane-strain tension). The initial sheet thickness is equal to 2 mm and an imperfection amplitude ξ of 0.1 % is considered ($\xi = (h_0^B - h_0^A)/h_0^B$). The neck spacing and orientation are fixed at $L_0/h_0 = 3$ and $\psi = 0$.

At the beginning of the simulation, the evolution of the strains in the two zones is similar. When the overall strain goes beyond 0.1, an acceleration of the deformation inside the imperfection zone is observed, while the strain in zone B gradually reaches a plateau. In the present case, the necking strain (strain at saturation outside the imperfection) is equal to 0.212.

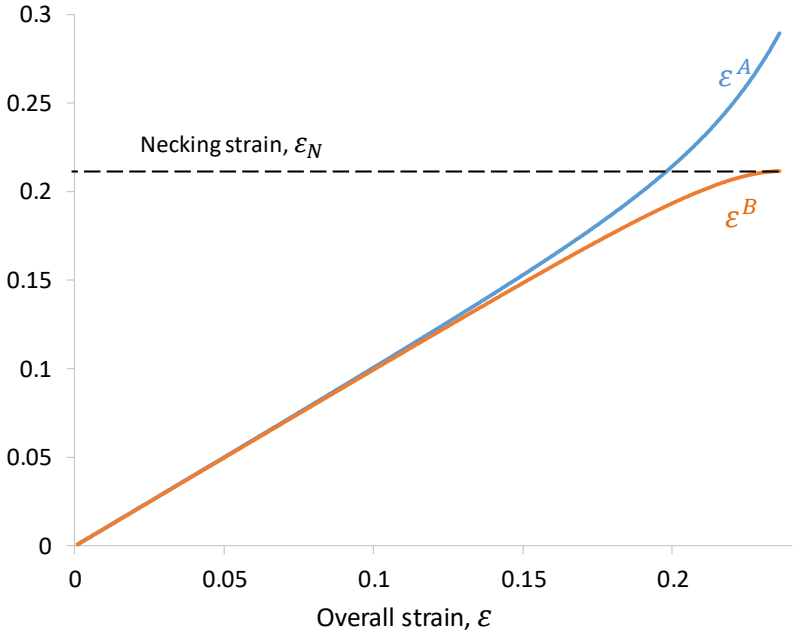

Fig. 3. Evolution of the strain inside (zone A) and outside the imperfection (zone B) as a function of the overall strain as predicted by the proposed two-zone model ($\varepsilon^B = \ln(F_{22}^B)$, $\varepsilon^A = \ln(F_{22}^A)$ and $\varepsilon = \ln(F_{22})$). The material has a rate-independent behaviour (40) with $\sigma_0 = 500$ MPa and $n = 0.1$. The parameters specifying the model are: $\rho_0 = 7800$ kg/m^3, $h_0 = 2$ mm, $\xi = 0.1\%$, $R = L_0^A/L_0 = 0.3$, $L_0/h_0 = 3$, $\psi = 0$, $\dot{F}_{22} = 5000$ s^{-1} and $\dot{F}_{11} = 0$.

The results shown in Fig. 3 have been obtained for a normalised neck spacing $L_0/h_0 = 3$. However, the neck spacing is not known a priori. Indeed, under dynamic loading, multiple necking patterns generally occur and the distance between necks is dependent on the loading rate (Shenoy and Freund, 1999; Mercier and Molinari, 2003; Zhou et al., 2006; Molinari et al., 2014; Zaera et al., 2015). To determine the critical neck spacing with the present model, it is necessary to carry out several simulations for different values of L_0/h_0 and to identify the value leading to the lowest necking strain. This approach is illustrated in Fig. 4 that shows the evolution of the necking strain (strain at saturation in zone B) as a function of the neck spacing. For the considered loading conditions, the necking strain reaches a minimum for $L_0^*/h_0 \sim 3.24$. The corresponding necking strain is $\varepsilon_N^* \sim 0.21$. It should be noted that the emergence of a critical neck spacing is related to the inclusion of the Bridgman correction factor in the modelling. Indeed, the increase in the necking strain for short wavelengths ($L_0 < L_0^*$) is due to stress triaxiality effects (Fressengeas and Molinari, 1994; Zaera et al., 2015), taken into account here via the Bridgman factor. If the Bridgman correction factor is switched

off, the necking strain is a monotonic function of the neck spacing and reaches its minimum (corresponding to the static necking strain) for $L_0 \to 0$ (Fig. 4).

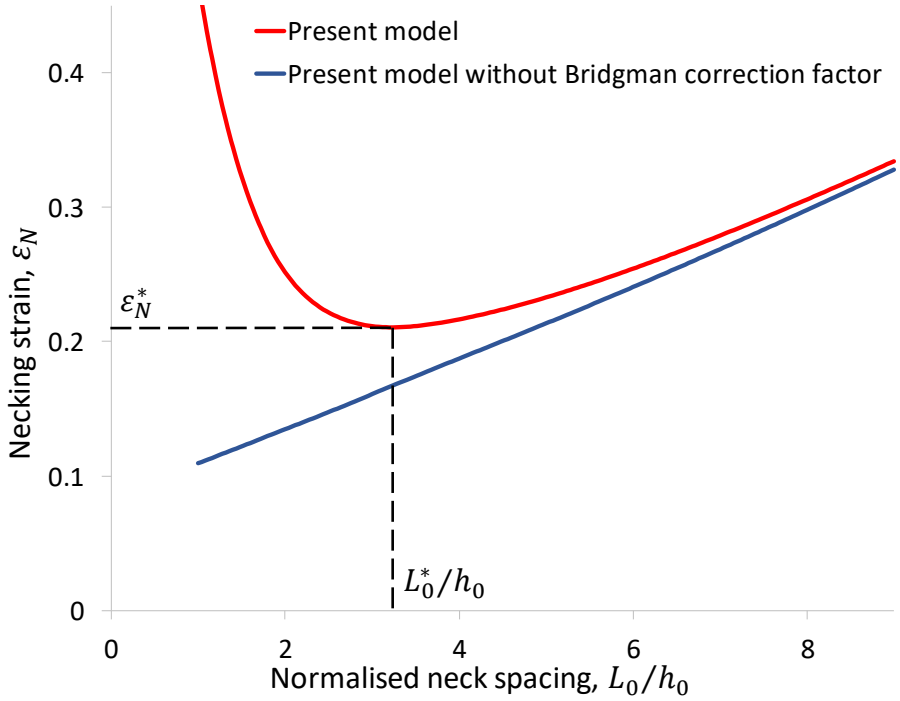

Fig. 4. Evolution of the necking strain as a function of the normalised neck spacing according to the proposed model. Results obtained with no Bridgman correction factor are also plotted. The material has a rate-independent behaviour (40) with $\sigma_0 = 500$ MPa *and* $n = 0.1$. *The parameters specifying the model are:* $\rho_0 = 7800$ kg/m^3, $h_0 = 2$ *mm*, $\xi = 0.1\%$, $R = L_0^A/L_0 = 0.3$, $\psi = 0$, $\dot{F}_{22} = 5000$ s^{-1} *and* $\dot{F}_{11} = 0$.

A similar minimisation method is applied to determine the critical imperfection orientation (value of ψ leading to the lowest necking strain[2]), see appendix A. Fig. 5-a presents the critical imperfection orientation ψ^* versus the loading path parameter $\chi = \dot{F}_{11}/\dot{F}_{22}$ for two values of the principal stretch rate: $\dot{F}_{22} = 100$ s^{-1} and $\dot{F}_{22} = 5000$ s^{-1}. It is reminded that ψ corresponds to the initial orientation of the imperfection (zone A). The imperfection rotates during the deformation of sheet. The current orientation $\bar{\psi}$ of the band (measured in the deformed configuration) is given by the following relation:

[2] Unless otherwise stated, the necking strain corresponds to the maximum principal value of the logarithmic strain tensor at saturation in zone B.

$$\bar{\psi} = \psi + \arctan\left(\frac{F_{\beta\alpha}}{F_{\alpha\alpha}}\right) \tag{41}$$

In his seminal analysis of sheet necking (under quasi-static loading), Hill (1952) showed that in the negative minor strain region, necks are aligned with the direction of zero stretch rate at the onset of necking and obtained the following expression for the neck orientation:

$$\bar{\psi}^{Hill} = arctan\left(-\sqrt{\bar{\chi}}\right) \tag{42}$$

where $\bar{\chi}$ is the strain-rate ratio, $\bar{\chi} = D_{11}/D_{22}$. Note that the strain-rate ratio $\bar{\chi}$ is not identical to the loading path parameter $\chi = \dot{F}_{11}/\dot{F}_{22}$. Indeed, it can be easily shown that $\bar{\chi} = \chi\, F_{22}/F_{11}$. Hence, with the loading conditions considered in the proposed model (see Eq. (2)), the strain-rate ratio $\bar{\chi}$ slightly increases during the computations. Fig. 5-b displays the evolution of the critical final neck orientation $\bar{\psi}^*$ obtained with the present model for two different values of the principal stretch rate ($\dot{F}_{22} = 100\ \mathrm{s}^{-1}$ and $\dot{F}_{22} = 5000\ \mathrm{s}^{-1}$) as a function of the strain-rate ratio $\bar{\chi}$ (the value reached at the end of the computations, when the neck is formed). The results are compared to the Hill critical neck orientation (42). In the biaxial expansion range ($\chi > 0$), the critical neck orientation $\bar{\psi}^*$ is always equal to zero (meaning that necks are perpendicular to the main straining direction). $\bar{\psi}^*$ becomes different to zero when the minor stretch rate $\dot{F}_{11}$ is negative. For both values of $\dot{F}_{22}$, the critical neck orientation predicted by the two-zone model is very close to the Hill angle. This means that the necking angle is not significantly affected by inertia effects. This finding is in agreement with the predictions of the linear stability analysis developed by Zaera et al. (2015) and the results of the expanding cylinder experiments of Zhang and Ravi-Chandar (2010).

(a)

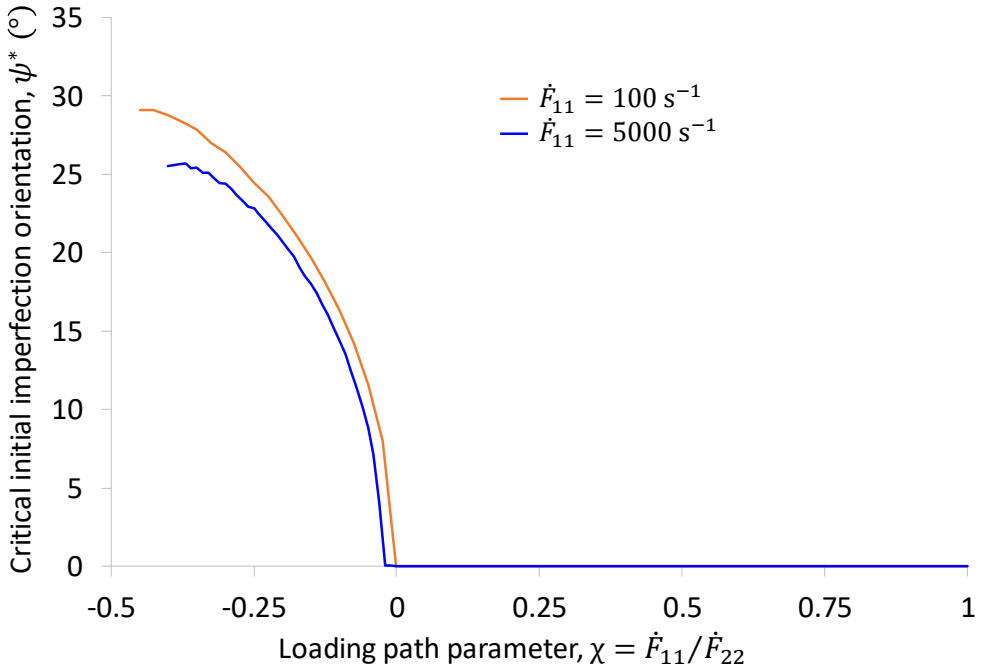

(b)

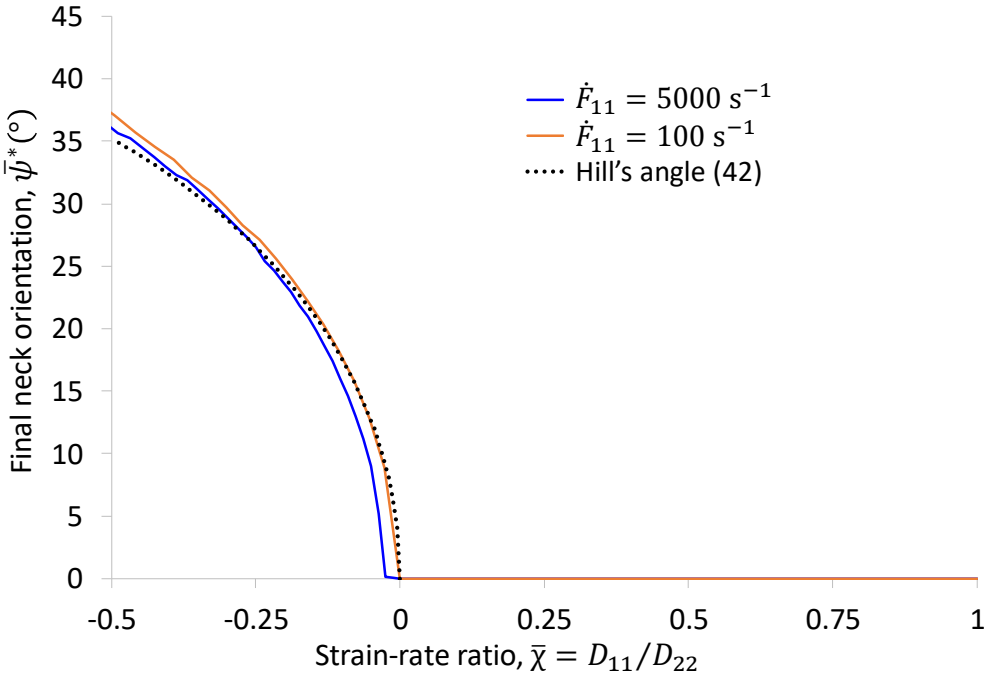

Fig. 5. (a) Evolution of the critical initial imperfection orientation with the loading path parameter. (b) Evolution of the final neck orientation predicted by the present model and the critical neck orientation derived from Hill's formula (42) with the strain rate ratio. Two values of the principal stretch rate are considered: $\dot{F}_{22} = 100\ \mathrm{s}^{-1}$ *and* $\dot{F}_{22} = 5000\ \mathrm{s}^{-1}$ *. The material has a rate-independent behaviour (40) with* $\sigma_0 = 500$ MPa *and* $n = 0.1$*. The parameters specifying the model are:* $\rho_0 = 7800\ \mathrm{kg/m^3}$, $h_0 = 2\ mm$, $\xi = 0.1\%$, $R = L_0^A/L_0 = 0.3$.

3. Results and analysis

3.1 Influence of the relative imperfection length and comparison with the finite element unit-cell simulations of Rodríguez-Martínez et al. (2017)

Under quasi-static loading, the predictions of Marciniak-Kuczyński-type models are generally independent of the sizes of the two zones (necking strains only depend on the relative thickness reduction in the imperfection zone). The same does not occur when inertia is taken into account. Indeed, the coefficient C_d (22), which characterises inertia effects, depends on $R = L_0^A/L_0$, the ratio of the imperfection length over the total cell length. R is also involved in the calculation of the Bridgman correction factor.

Fig. 6 shows the evolution of the necking strain[3] with the neck spacing for different values of R ranging between 0.2 and 0.3. The loading conditions correspond to plane strain tension ($\chi = 0$) and an initial effective strain-rate of 10000 s^{-1}. The material has a viscoplastic behaviour described by the following relation

$$\bar{\sigma} = \sigma_0 \left(\frac{\dot{\bar{\varepsilon}}}{\dot{\varepsilon}_r}\right)^m \tag{43}$$

with $\sigma_0 = 500$ MPa, $m = 0.01$ and $\dot{\varepsilon}_r = 1000\ s^{-1}$. The imperfection amplitude is $\xi = 2\%$. The results derived from the two-zone model appear to be quite sensitive to the value of R used in the calculations. The critical neck spacing and the associated necking strain increase for decreasing values of R. In Fig. 5, the predictions of the two-zone model are compared to the results of the unit-cell finite element simulations[4] of Rodríguez-Martínez et al. (2017). It appears that there is an "optimal" value $R = 0.28$ that allows the achievement of an excellent agreement between the two approaches in the whole range of neck spacings considered.

[3] In order to be consistent with the data presented in (Rodríguez-Martínez et al., 2017), in Figs. 5-8, the necking strain corresponds to the effective plastic strain at saturation in zone B.

[4] The configuration considered in the simulations of Rodríguez-Martínez et al. (2017) is a unit periodic cell of a plate having an initial sinusoidal geometric imperfection. The cell size corresponds to the imperfection wavelength and is denoted by L_0. In most cases, localisation takes place at the centre of the cell where the initial thickness is minimum. Therefore, the neck spacing is identical to the imperfection wavelength.

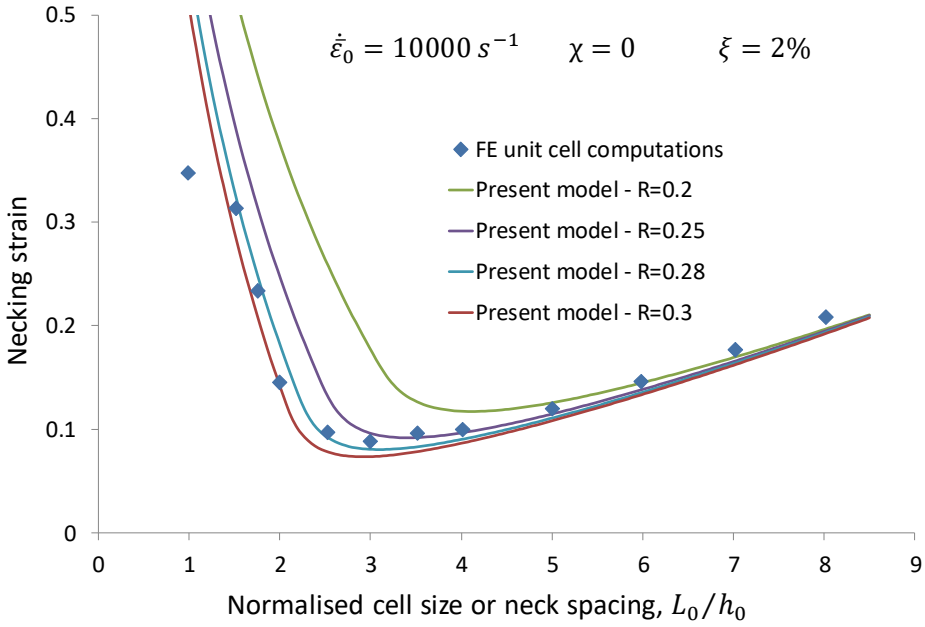

Fig. 6. Evolution of the necking strain with the normalised neck spacing as predicted by the two-zone model for several values of the relative imperfection length $R = L_0^A/L_0$. *The results of the numerical simulations of Rodríguez-Martínez et al. (2017) are also plotted. The material has a viscoplastic behaviour (43) with* $\sigma_0 = 500$ MPa, $m = 0.01$ *and* $\dot{\varepsilon}_r = 1000\ \mathrm{s}^{-1}$. *Loading conditions:* $\dot{\bar{\varepsilon}}_0 = 10000\ \mathrm{s}^{-1}$, $\chi = 0$. *Other parameters are set at* $\rho_0 = 7800\ \mathrm{kg/m}^3$, $h_0 = 2$ mm *and* $\xi = 2\%$.

In order to assess if this "optimal" value of R is still appropriate for other configurations and loading conditions, additional comparisons with the results of Rodríguez-Martínez et al. (2017) have been made and are presented in Figs. 7-9. Fig. 7 shows the relation between necking strain and neck spacing for several imperfection amplitudes ξ. Fig. 8 displays the influence of the applied initial effective strain-rate $\dot{\bar{\varepsilon}}_0$ and Fig. 9 of the loading path parameter χ. In all cases, the necking strains predicted by the proposed model (with $R = 0.28$) are in good agreement with the results of the unit-cell finite element simulations of Rodríguez-Martínez et al. (2017). This agreement suggests that, despite its simplicity, the two-zone model captures the main physical mechanisms that control plastic flow localisation under dynamic loading.

All the results reported in the rest of the paper have been obtained with $R = 0.28$.

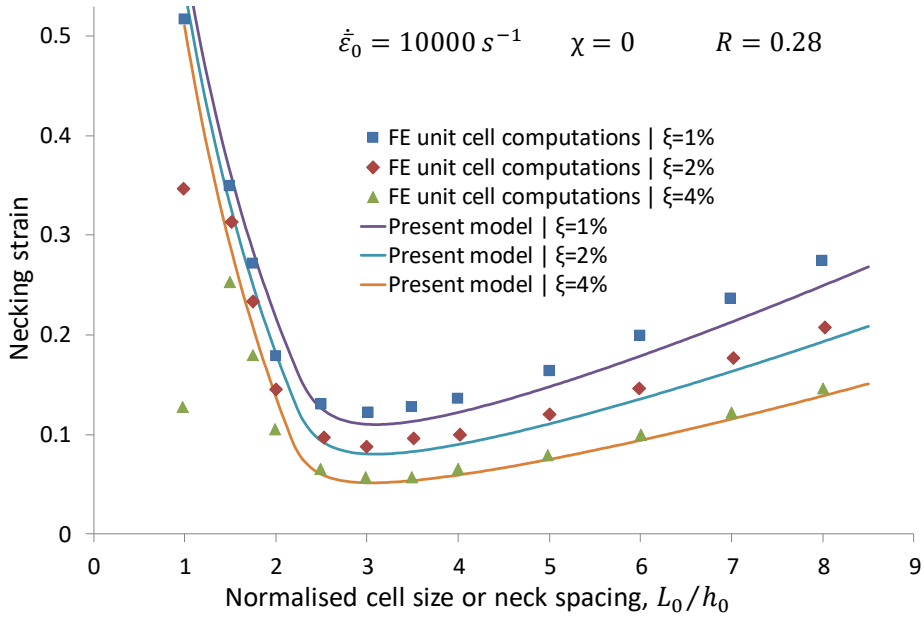

Fig. 7. Necking strain versus neck spacing for several values of the imperfection amplitude $\xi = 1\%; 2\%$ *and* $4\ \%$*. Comparison between the results of the present model (with* $R = 0.28$*) and of the finite element unit-cell simulations of Rodríguez-Martínez et al. (2017). Other parameters are identical to those adopted in Fig. 6.*

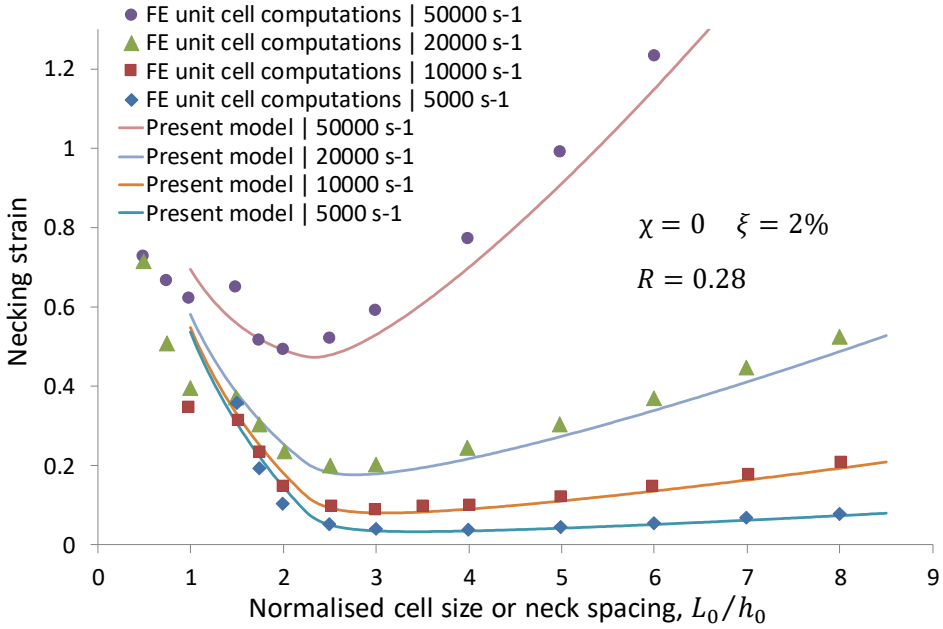

Fig. 8. Necking strain versus neck spacing for several values of the initial effective strain-rate $\dot{\bar{\varepsilon}}_0$ =5000 s^{-1}; 10000 s^{-1}; 20000 s^{-1} and 50000 s^{-1}*. Comparison between the results of the present model (using* $R = 0.28$*) and of the finite element unit-cell simulations of Rodríguez-Martínez et al. (2017). Other parameters are identical to those adopted in Fig. 6.*

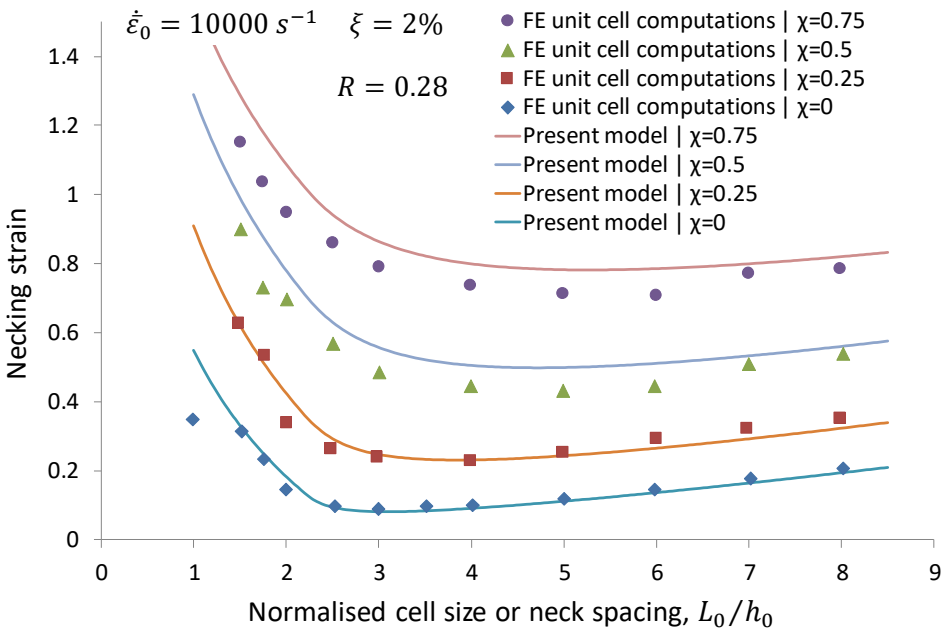

Fig. 9. Necking strain versus neck spacing for several values of the loading path parameter χ=0; 0.25; 0.5 *and* 0.75. *Comparison between the results of the present model (with* $R = 0.28$*) and of the finite element unit-cell simulations of Rodríguez-Martínez et al. (2017). Other parameters are identical to those adopted in Fig. 6.*

3.2 Influence of inertia and loading conditions

In this section, the influence of inertia on ductility is investigated. A rate-independent material obeying the J_2 flow theory is considered. Hardening is described by a power law relation (40) with $n = 0.1$ and $\sigma_0 = 500$ MPa. Fig. 10 shows the evolution of the major necking strain (maximum principal logarithmic strain at saturation in zone B for the critical neck spacing and orientation) with the applied principal stretch rate for different loading paths. The predictions of the dynamic two-zone model are compared to the results of the finite element simulations of plate necking presented in Appendix B. As expected, the necking strain increases with the stretch rate. As a rate-independent material is considered, this increase in necking strain is only due to inertia effects. One can also observe that the influence of inertia is more pronounced for loading paths where $\chi \leq 0$. Indeed, for $\chi = -0.1$ and $\chi = 0$, the necking strain increases in the whole range of stretch rates considered. For $\chi = 0.25$ and $\chi = 0.5$, the effect of inertia becomes visible only when the stretch rate becomes larger than 1000 s^{-1}. A very good agreement between the analytical model and the finite element analyses is observed for all the considered loading paths and stretch rates.

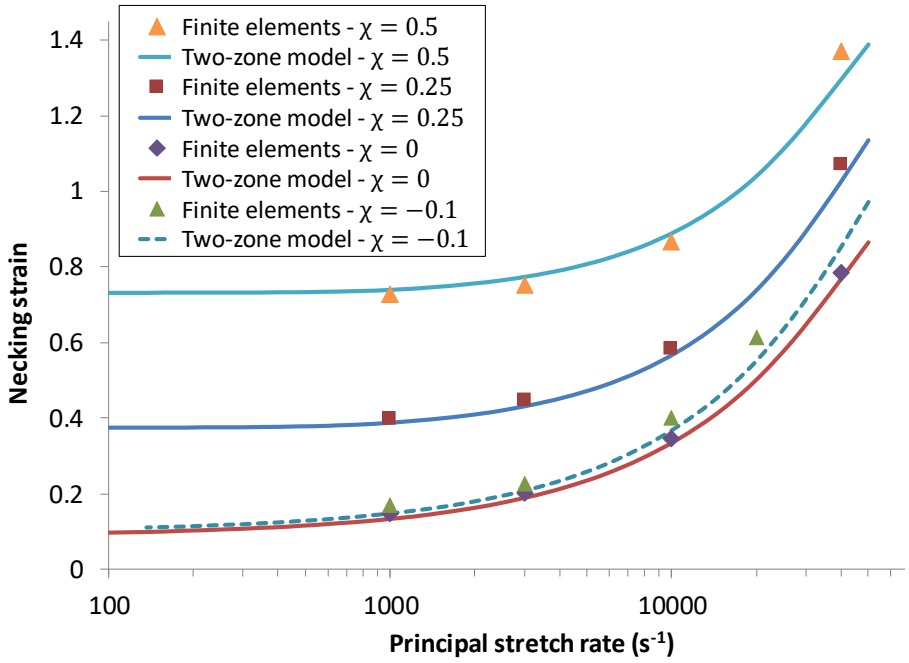

Fig. 10. Evolution of the necking strain (for the critical neck spacing and orientation) with the overall principal stretch rate $\dot{F}_{22}$ *for different loading paths,* $\chi = -0.1$*,* $\chi = 0$*,* $\chi = 0.25$ *and* $\chi = 0.5$*. The results obtained with the two-zone model are compared to the results of the finite element simulations presented in Appendix B. The material has a rate-independent behaviour (40) with* $\sigma_0 = 500$ MPa *and* $n = 0.1$*. Other parameters are set at* $\rho_0 = 7800$ kg/m^3*,* $h_0 = 2$ mm*,* $\xi = 0.05\%$*,* $R = 0.28$*.*

It should be noted that the increase in necking strain due to inertia is dependent on the sheet thickness. As an illustration, Fig. 11 displays the evolution of the necking strain with the principal stretch rate for different values of the initial sheet thickness ($h_0 = 1; 2$ and 4 mm). As expected, the increase in the necking strain with the stretch rate is more pronounced for thicker sheets. In fact, for a rate-independent solid, the influence of inertia can be characterised by a non-dimensional number, see for e.g. (Xue et al., 2008),

$$I = \frac{\dot{F}_{22} h_0}{\sqrt{\sigma_0/\rho_0}}, \tag{44}$$

which depends on the prescribed stretch rate $\dot{F}_{22}$, the plate thickness h_0, the mass density ρ_0 and the reference flow stress σ_0.

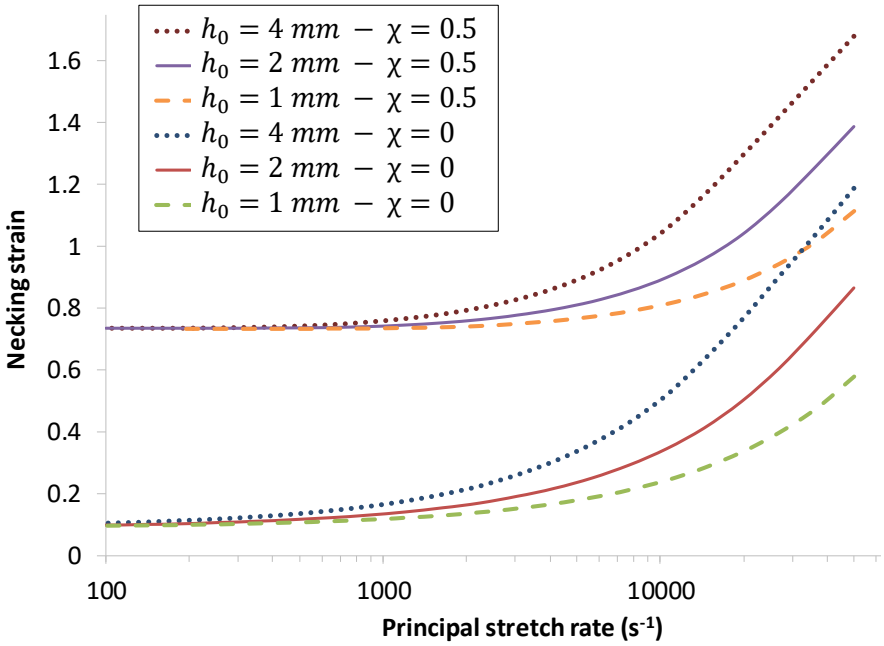

Fig. 11. Influence of the sheet thickness h_0 on the evolution of the necking strain with the principal stretch rate for two loading paths, $\chi = 0$ and $\chi = 0.5$. Other model parameters are identical to those adopted in Fig. 10.

Fig. 12 presents forming limit curves obtained for three values of the principal stretch rate, $\dot{F}_{22} = 1000\ \mathrm{s}^{-1}$, $\dot{F}_{22} = 3000\ \mathrm{s}^{-1}$ and $\dot{F}_{22} = 10000\ \mathrm{s}^{-1}$. The major and minor strains correspond respectively to the maximum and minimum in-plane principal values of the logarithmic strain tensor at saturation in zone B for the critical neck spacing and orientation. When the prescribed stretch rate is increased, the FLD is shifted upwards. The increase in ductility due to inertia effects is visible for all loading paths, but is more pronounced in the negative minor strain region. One can also observe that, for a given stretch-rate, the lowest necking strain is obtained for plane strain tension ($\chi = 0$). This result is consistent with the findings of Zaera et al. (2015). Using a linear stability analysis, these authors have also observed that plane strain conditions lead to the most unstable material conditions, irrespectively of the loading rate.

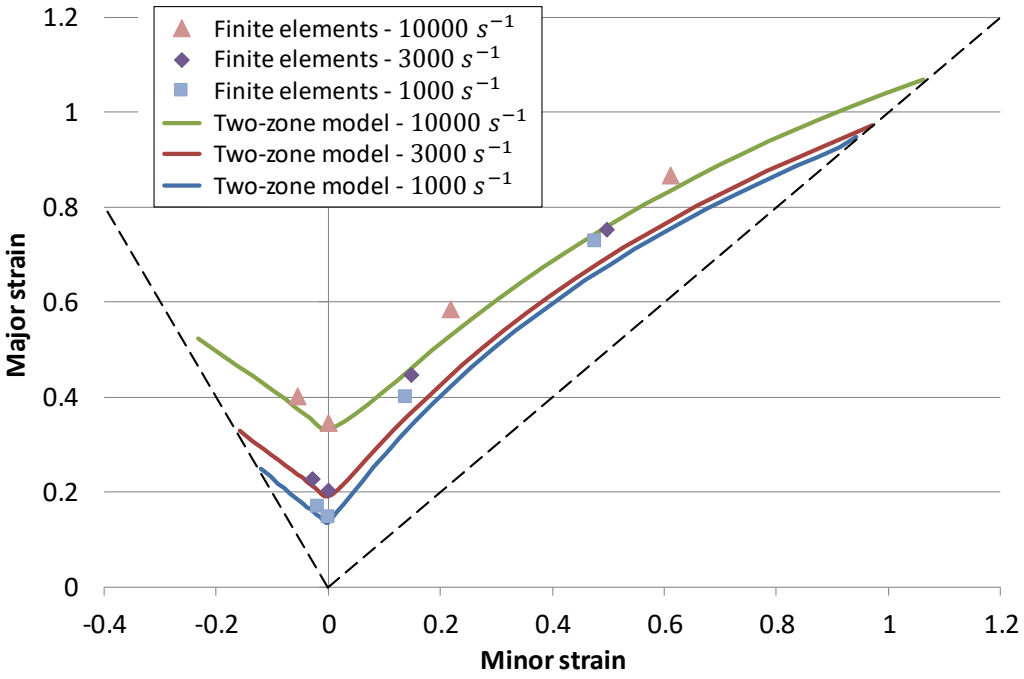

Fig. 12. Forming limit curves obtained with the two-zone model and the finite element computations presented in Appendix B for three values of the principal stretch rate, $\dot{F}_{22} = 1000\ \mathrm{s}^{-1}$, $\dot{F}_{22} = 3000\ \mathrm{s}^{-1}$ *and* $\dot{F}_{22} = 10000\ \mathrm{s}^{-1}$. *The model parameters are identical to those adopted in Fig. 10.*

3.3 Influence of the imperfection amplitude

The predictions of the two-zone model are dependent on the imperfection amplitude considered. The results presented in Figs. 10-12 have been obtained with a relative thickness reduction in zone A of $\xi = 0.05\%$. This value has been selected because it provides a good agreement with the finite element simulations. Indeed, the random geometric imperfection considered in the numerical simulations (see Appendix B) is very different to the imperfection considered in the two-zone model (homogeneous thickness reduction in zone A). Therefore, it is difficult to choose a priori a value for ξ. However, it should be noted that for $\xi = 0.05\%$ the initial thickness reduction in zone A ($h_0^B - h_0^A = 1$ µm) is of the same order that the root mean squared roughness of the plate free surfaces in the finite element model ($R_q = 2.88$ µm, see appendix B). Moreover, Fig. 13 shows that the influence of the imperfection amplitude on the necking strain in the two-zone model and in the finite element model are similar.

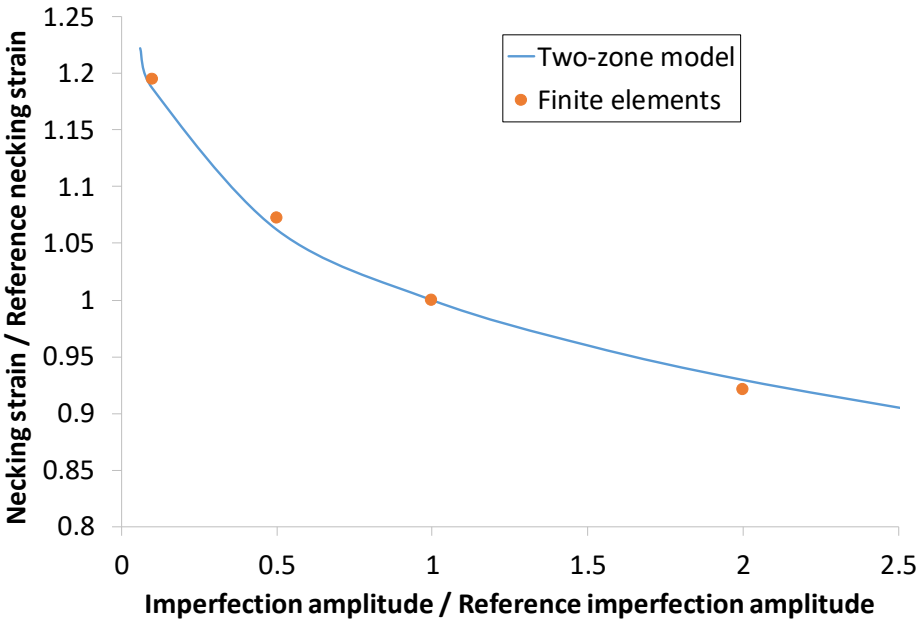

Fig. 13. Evolution of the necking strain (normalised by the necking strain obtained with a reference imperfection amplitude) with the imperfection amplitude (normalised by the reference imperfection amplitude). The reference amplitude is $\xi_{ref} = 0.05\%$ *for the two-zone model and* $\eta_{ref} = 10$ µm *for the finite element model. Loading conditions:* $\dot{F}_{22} = 1000\ \mathrm{s}^{-1}$ *and* $\dot{F}_{11} = 0$*. Other model parameters are identical to those adopted in Fig. 10.*

Fig. 14 shows forming limit curves obtained using the two-zone model for two imperfection amplitudes and two values of the principal stretch rate. It appears that the influence of the imperfection amplitude is more marked in the positive minor strain region ($\chi > 0$) and for the largest stretch rate ($\dot{F}_{22} = 10000\ \mathrm{s}^{-1}$).

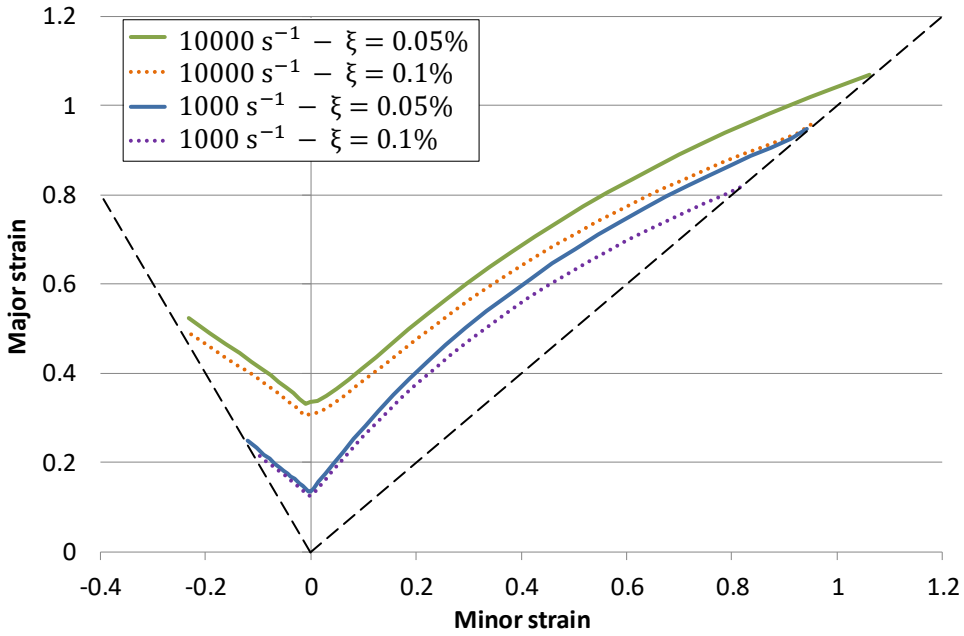

Fig. 14. Influence of the imperfection magnitude on the predictions of the two-zone model. Forming limit curves obtained for two different imperfection amplitudes, $\xi = 0.05\%$ and $\xi = 0.1\%$, and two values of the principal stretch rate, $\dot{F}_{22} = 1000\ \mathrm{s}^{-1}$ and $\dot{F}_{22} = 10000\ \mathrm{s}^{-1}$, are presented. Other model parameters are identical to those adopted in Fig. 10.

3.4 Viscoplastic materials

The aim of the present section is to analyse the influence of material strain-rate sensitivity on necking strains. Fig. 15 presents a comparison between the evolution of the major necking strain with the principal stretch rate for a viscoplastic solid and for a rate-independent solid. The behaviour of the viscoplastic solid is described by an additive over-stress relation,

$$\bar{\sigma} = \sigma_0 \left(\bar{\varepsilon}^n + K_2 \left(\frac{\dot{\bar{\varepsilon}}}{\dot{\varepsilon}_r} \right)^{m_2} \right), \tag{45}$$

with $\sigma_0 = 500$ MPa, $n = 0.1$, $m_2 = 0.05$, $K_2 = 1$, and $\dot{\varepsilon}_r = 1000\ \mathrm{s}^{-1}$. The rate-independent solid corresponds to $K_2 = 0$. For the two loading paths considered in Fig. 15 ($\chi = 0$ and $\chi = 0.25$), at the lowest stretch-rate ($\dot{F}_{22} = 100\ \mathrm{s}^{-1}$), the necking strain of the viscoplastic solid is larger than that of the rate-independent material. For $\dot{F}_{22} = 100\ \mathrm{s}^{-1}$, inertia effects are negligible. Therefore, the difference between the necking strains of the viscoplastic and rate-independent materials is due to a stabilising effect of strain-rate sensitivity. The necking strain increases with the principal stretch-rate for both materials. However, the curves of the viscoplastic and rate-independent solids become closer and closer when the stretch-rate

increases and intersect for $\dot{F}_{22} \approx 10000\ \mathrm{s}^{-1}$. At larger stretch-rates, the necking strain of the viscoplastic material is smaller than that of the rate-independent material. This phenomenon is also predicted by the finite element computations. The results presented in Fig. 15 show that strain-rate sensitivity does not necessarily lead to an increase in ductility. This observation may seem surprising at first sight but a similar behaviour has been observed by Vadillo et al. (2012) in the case of the dynamic expansion of thin rings. Using linear stability analysis and finite element simulations, these authors found that "under certain loading conditions decreasing rate sensitivity may not lead to a more unstable material". In fact, under dynamic loading there is a complex interplay between inertia and strain-rate sensitivity. Increasing rate sensitivity generally reduces inertia effects and may promote flow instabilities.

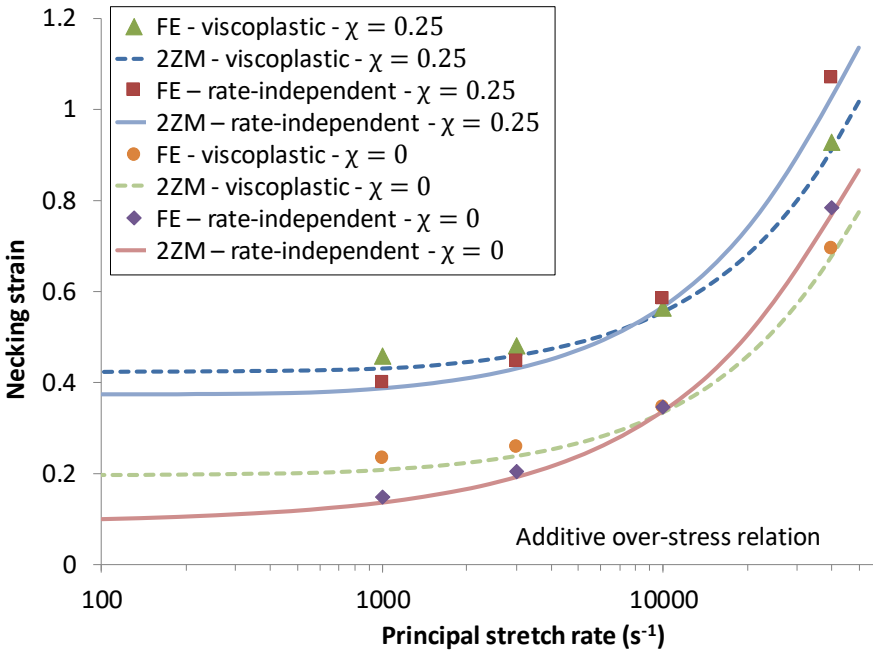

Fig. 15. Evolution of the necking strain (for the critical neck spacing and orientation) with the principal stretch rate for a viscoplastic solid and a rate-independent solid for two loading paths, $\chi = 0$ *and* $\chi = 0.25$. *Results obtained using the two-zone model (2ZM), and the finite element simulations described in Appendix B (FE) are presented. The behaviour of the viscoplastic solid is described by an additive over-stress relation (45) with* $\sigma_0 = 500$ MPa, $n = 0.1$, $m_2 = 0.05$, $K_2 = 1$, *and* $\dot{\varepsilon}_r = 1000\ \mathrm{s}^{-1}$. *The rate-independent case corresponds to* $K_2 = 0$. *Other parameters are set at* $\rho_0 = 7800\ \mathrm{kg/m}^3$, $h_0 = 2$ mm, $\xi = 0.05\%$, $R = 0.28$.

The influence of strain-rate sensitivity depends strongly on the parameters of the constitutive relation. For instance, Fig. 16 presents the evolution of the necking strain with the principal stretch rate for two values of the exponent of the additive over stress relation (45), $m_2 = 0.02$ and $m_2 = 0.05$, and for two strain paths, $\chi = 0$ and $\chi = 0.25$. The curves for the corresponding rate-independent material ($K_2 = 0$) are also plotted. When $m_2 = 0.02$, strain-rate sensitivity has a detrimental effect on ductility for almost all the stretch rates considered. The necking strain of the viscoplastic material is generally smaller than that of the rate-independent solid. This effect is more pronounced when $\chi = 0.25$. For the lowest stretch rate considered in Fig. 16 ($\dot{F}_{22} = 100\ \mathrm{s}^{-1}$), inertia effects are negligible. It therefore appears that even under quasi-static conditions, strain-rate sensitivity may have a detrimental effect on formability. A similar conclusion has been reported in several studies based on experimental or theoretical analyses (Lee et al., 2008; Verleysen et al., 2011; Chu et al., 2014).

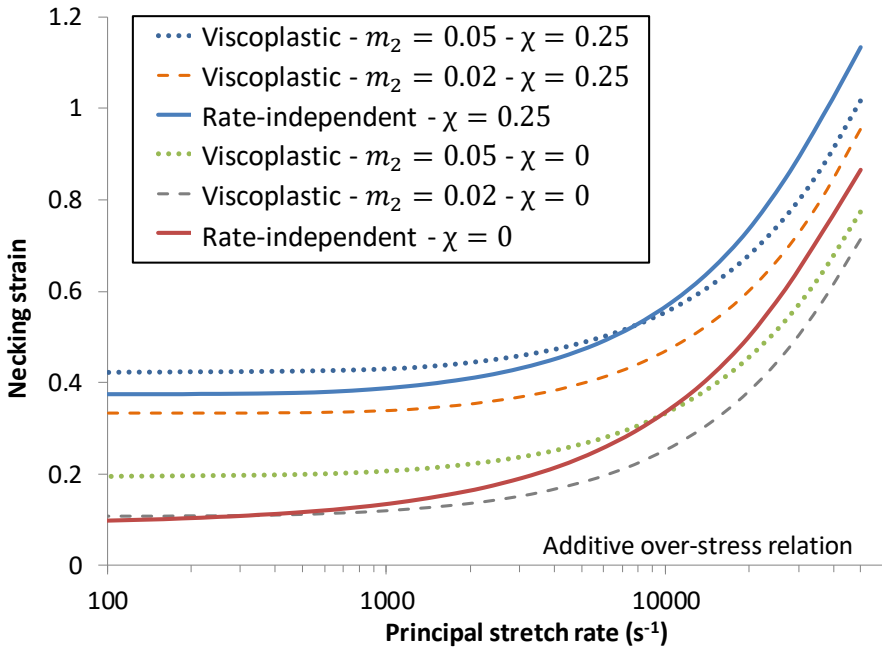

Fig. 16. Influence of the strain-rate sensitivity exponent m_2 of the additive over-stress relation (45) on the evolution of the necking strain with the prescribed stretch rate. The results obtained for a rate-independent solid ($K_2 = 0$) are also presented. Other parameters are as in Fig. 15.

Some calculations have been performed with other constitutive relations. Fig. 17 presents necking strain versus stretch rate curves obtained with a multiplicative over-stress relation,

$$\bar{\sigma} = \sigma_0 \bar{\varepsilon}^n \left(1 + K_3 \left(\frac{\dot{\bar{\varepsilon}}}{\dot{\varepsilon}_r}\right)^{m_3}\right), \tag{46}$$

and Fig. 18 presents results obtained using a power law relation,

$$\bar{\sigma} = \sigma_0 \bar{\varepsilon}^n \left(\frac{\dot{\bar{\varepsilon}}}{\dot{\varepsilon}_r}\right)^{m_0}. \tag{47}$$

With the multiplicative over-stress relation, a destabilising effect of strain-rate sensitivity is observed at high loading rate. When the stretch rate goes beyond a certain value, the necking strain of the viscoplastic material becomes lower than that of the rate-independent material (Fig. 17). The same does not occur with the power law relation (Fig. 18). In this case, irrespective of the value of the strain-rate sensitivity exponent m_0, the necking strain of the viscoplastic material is always greater than that obtained with the rate-independent solid. The results presented in Figs. 15-18 are consistent with the findings of Vadillo et al. (2017) who observed a destabilising effect of rate sensitivity only for materials with a non-constant logarithmic rate sensitivity (which is the case for the two over-stress relations but not for the power law model).

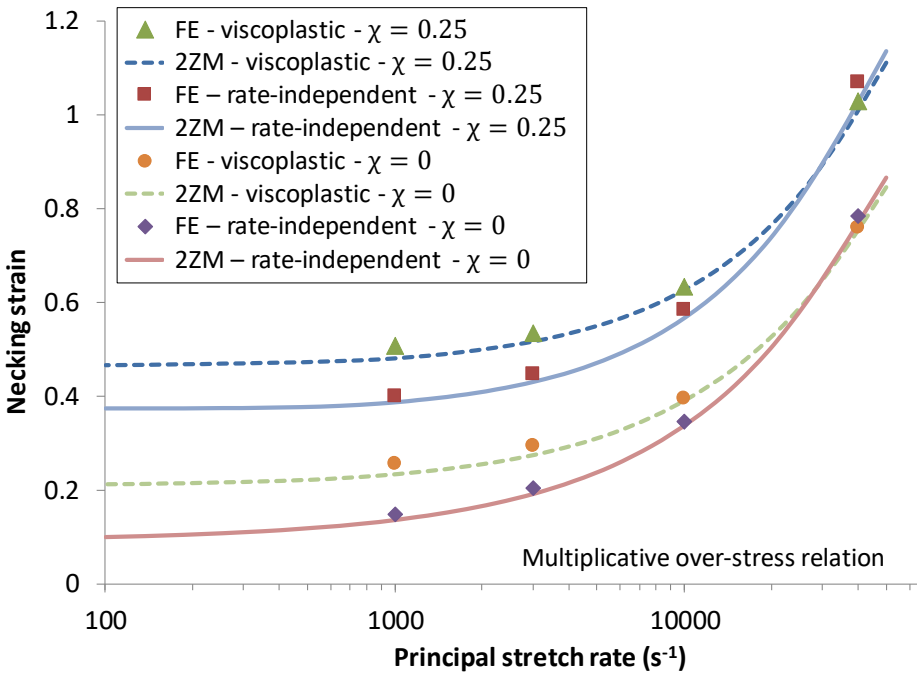

Fig. 17. Evolution of the necking strain (for the critical neck spacing and orientation) with the principal stretch rate for a viscoplastic solid and a rate-independent solid for two loading paths, $\chi = 0$ and $\chi = 0.25$. Results obtained using the two-zone model (2ZM), and the finite element simulations described in Appendix B (FE) are presented. The behaviour of the viscoplastic solid is described by a multiplicative over-stress relation (46) with $\sigma_0 = 500$ MPa, $n = 0.1$, $m_3 = 0.05$, $K_3 = 0.5$, and $\dot{\varepsilon}_r =$

$1000\ \mathrm{s}^{-1}$. *The rate-independent case corresponds to* $K_3 = 0$. *Other parameters are set at* $\rho_0 = 7800\ \mathrm{kg/m}^3$, $h_0 = 2\ mm$, $\xi = 0.05\%$, $R = 0.28$.

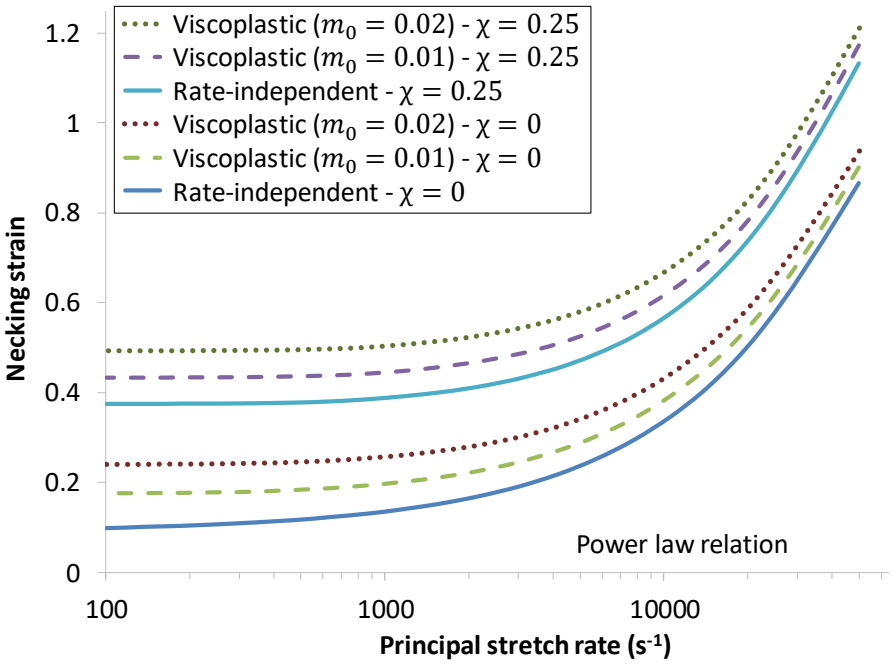

Fig. 18. Evolution of the necking strain (for the critical neck spacing and orientation) with the principal stretch rate for viscoplastic solids and a rate-independent solid for two loading paths, $\chi = 0$ *and* $\chi = 0.25$, *according to the dynamic two-zone model. The behaviour of the viscoplastic solids is described by a power law relation (47) with* $\sigma_0 = 500$ MPa, $n = 0.1$, *and* $\dot{\varepsilon}_r = 1000\ \mathrm{s}^{-1}$; *two values of the rate sensitivity exponent are considered:* $m_0 = 0.01$ and $m_0 = 0.02$. *The rate-independent case corresponds to* $m_0 = 0$. *Other parameters are set at* $\rho_0 = 7800\ \mathrm{kg/m}^3$, $h_0 = 2$ mm, $\xi = 0.05\%$, $R = 0.28$.

3.5 Influence of yield surface shape

The results presented in the previous sections have been obtained using the J_2 flow theory. It is well known that predictions of plastic flow instabilities are very sensitive to the assumed constitutive model and in particular to the yield criterion (Stören and Rice, 1975; Barlat, 1987; Ferron and Molinari, 1989; Kuroda and Tvergaard, 2000; Dequiedt, 2010, 2011, N'souglo et al., 2019). For quasi-static loading conditions, numerous works have been carried out to implement complex constitutive models in Marciniak-Kuczyński-type models, see Section 1. In this section, a preliminary analysis of the influence of yield surface shape on necking under dynamic loading is presented. The Cazacu and Revil-Baudard (2017) strain-

rate potential (CR2017 SRP) described in Section 2.3 is considered (more complex constitutive models will be considered in future investigations). Fig. 19 presents the yield surface associated with the CR2017 SRP for several values of the parameter β=0, 0.21 and 0.35. With β=0, the Mises yield surface is retrieved. The value β=0.21 (resp. β=0.35) was chosen because the yield surface is, in this case, almost identical to that corresponding to the Hosford (1972) criterion with $n = 6$ (resp. $n = 8$), which is a typical value for BCC (resp. FCC) metals.

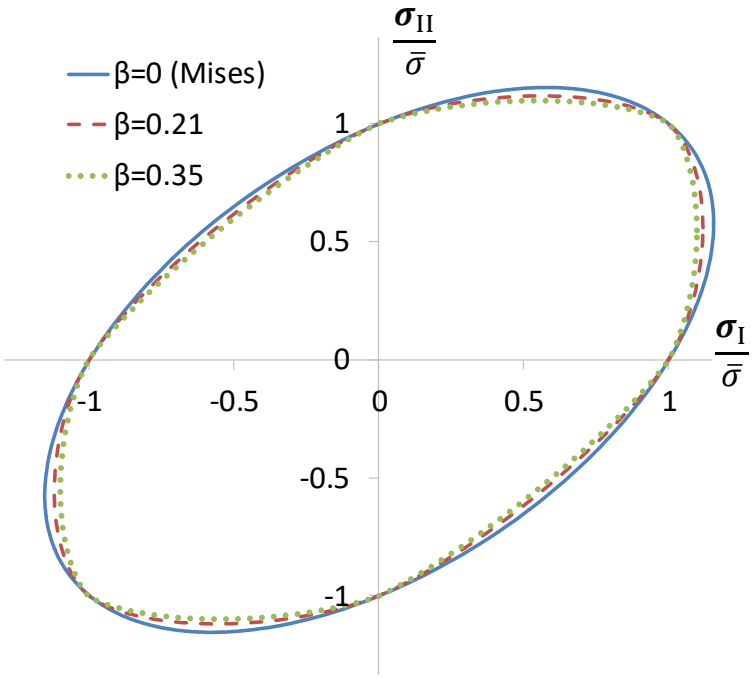

Fig. 19. Yield surface associated to the Cazacu and Revil-Baudard (2017) strain-rate potential (28) for several values of the parameter β=0, 0.21 *and* 3.35.

The forming limit curves obtained with the CR2017 SRP for β=0, 0.21 and 0.35 and for two values of principal stretch rate, $\dot{F}_{22} = 1000\ s^{-1}$ and $10000\ s^{-1}$, are presented in Fig. 20. The material has a rate-independent behaviour. The influence of yield surface shape is visible only in the positive minor strain region. When the parameter β is changed from 0 to 0.21, a significant decrease in the necking strains for loading paths close to equi-biaxial extension is observed. For β=0.35, the maximal necking strain is no longer obtained for equi-biaxial extension. This behaviour can be explained from the shape of the yield surfaces shown in Fig. 19. Indeed, the curvature of the yield surface in the vicinity of the point corresponding to equi-biaxial extension increases with the value of β. This increase in the yield surface

curvature is likely to promote plastic flow instabilities. From Fig. 20, it also appears that the influence of inertia becomes more marked for certain loading paths when β increases. Indeed, when the stretch rate goes from 1000 s^{-1} to 10000 s^{-1}, the necking strain in equi-biaxial extension increases by only 11% (from 0.95 to 1.07) for β=0, while it increases by 33% (from 0.36 to 0.48) for β=0.35. These results show that inertia effects are enhanced when a "less stable" material behaviour is considered.

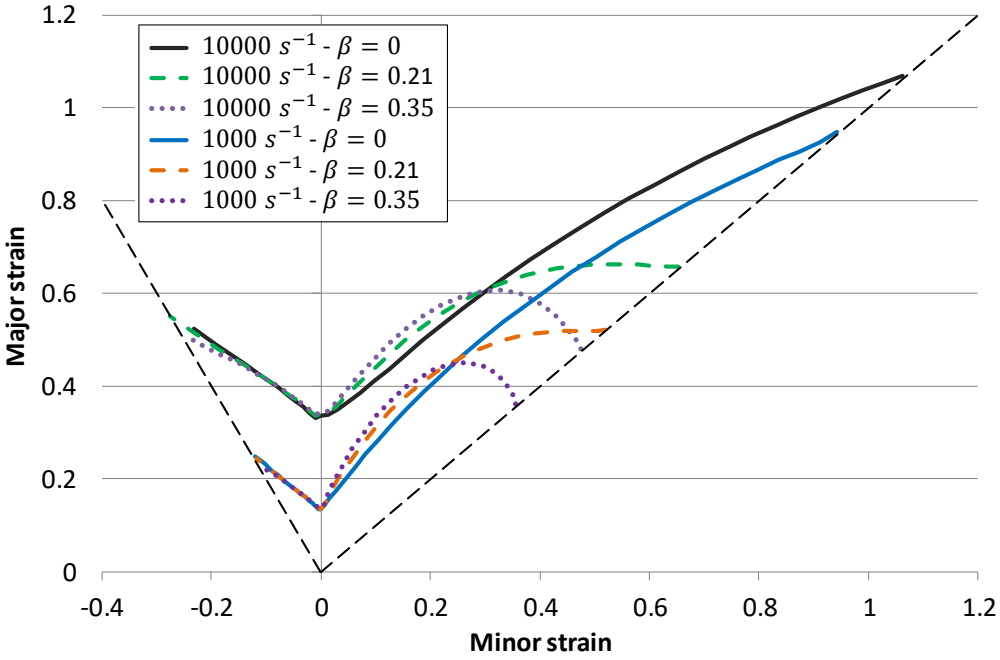

Fig. 20. Forming limit diagrams obtained for three values of the parameter β of the Cazacu and Revil-Baudard (2017) strain-rate potential (28) and two values of the principal stretch rate, $\dot{F}_{22} = 1000\ s^{-1}$ and $\dot{F}_{22} = 10000\ s^{-1}$. The material has a rate-independent behaviour (40) with $\sigma_0 = 500$ MPa and $n = 0.1$. Other parameters are set at $\rho_0 = 7800\ \mathrm{kg/m^3}$, $h_0 = 2\ mm$, $\xi = 0.05\%$, $R = 0.28$.

3.6 Comparison with the experimental results of Golovashchenko et al. (2013)

Golovashchenko et al. (2013) investigated the formability of different grades of dual phase steel (DP500, DP590, DP780 and DP980) under quasi-static and dynamic loading conditions. They compared the strains achieved in electrohydraulic forming (EHF) and quasi-static forming experiments and observed a significant improvement in formability under EHF conditions. Fig. 21 presents a comparison between experimental results for DP590 steel and forming limit diagrams (FLDs) obtained with the two-zone model. The EHF data points

corresponds to experiments where 1 mm thick circular specimens were formed into a 34° conical die. The quasi-static (QS) data points were obtained using the limiting dome height technique. Golovashchenko et al. (2013) carried out numerical simulations of the EHF conical die experiments and observed that the strain rate in the specimen reaches values ranging between 2000 s^{-1} and 10000 s^{-1}. The theoretical FLDs presented in Fig. 21 were obtained using the Cazacu and Revil-Baudard (2017) strain-rate potential with $\beta = 0.21$ (representative value for BCC metals) and the Johnson-Cook hardening model:

$$\bar{\sigma} = (A + B.\bar{\varepsilon}^n).\left(1 + C.\ln\left(\frac{\dot{\bar{\varepsilon}}}{\dot{\varepsilon}_r}\right)\right) \tag{48}$$

with $A = 392$ MPa, $B = 697$ MPa, $n = 0.4$, $C = 0.0153$ and $\dot{\varepsilon}_r = 0.02\ s^{-1}$ (Hassannejadasl et al., 2014). In addition to the two "dynamic" FLDs obtained for $\dot{F}_{22} = 2000\ s^{-1}$ and $\dot{F}_{22} = 10000\ s^{-1}$, Fig . 21 also displays a quasi-static FLD, which have been obtained with a rate-independent behaviour ($C = 0$ in Eq. (48)) and a low stretch rate of $\dot{F}_{22} = 100\ s^{-1}$, such as inertia effects are negligible.

A fairly good agreement between modelling and experiments is observed. The upward shift of the forming limit diagram predicted by the two-zone model (caused by inertia and strain-rate sensitivity effects) is consistent with the increase in ductility achieved in the EHF experiments.

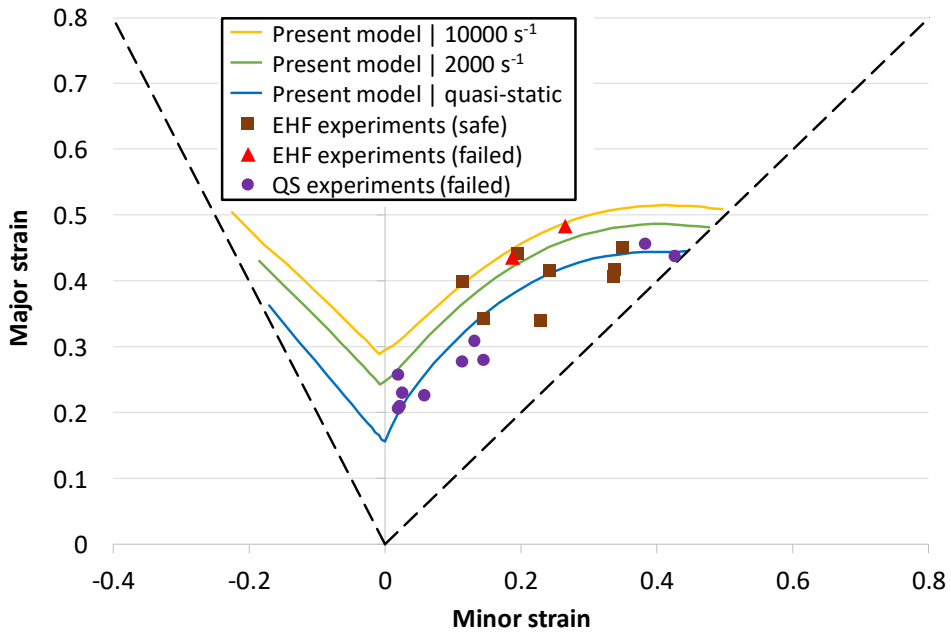

Fig. 21. Comparisons between forming limit diagrams obtained with the two-zone model and results of the electrohydraulic (EHF) and quasi-static (QS) formability experiments of Golovashchenko et al. (2013). The material behaviour is described by the Cazacu and Revil-Baudard (2017) strain-rate potential with $\beta = 0.21$ *and the Johnson-Cook hardening model (48) with* $A = 392\ MPa$, $B = 697\ MPa$, $n = 0.4$, $C = 0.0153$ *and* $\dot{\varepsilon}_r = 0.02\ s^{-1}$. *The quasi-static forming limit curve was obtained with a rate-independent behaviour (*$C = 0$*) and a low stretch rate of* $\dot{F}_{22} = 100\ s^{-1}$. *Other parameters are set at* $\rho_0 = 7800\ \mathrm{kg/m^3}$, $h_0 = 1\ mm$, $\xi = 0.5\%$ *and* $R = 0.28$.

4. Conclusions

The present paper deals with the modelling of necking localisation in plates subjected to dynamic biaxial loading. An extension of the two-zone model introduced by Marciniak and Kuczyński (1967) and Hutchinson and Neale (1978a) to include inertia effects is proposed. Inertia is taken into account by using the virtual work principle together with the simplified kinematic assumptions of the two-zone approach. Stress triaxiality effects are also taken into account with the use of the Bridgman correction factor. The resulting model is simple and easy to implement; limit strains (at the onset of localised necking) are obtained via numerical integration of a system of two ordinary differential equations.

The model involves an adjustable parameter, the ratio of the initial imperfection length to the initial total cell length. A suitable value of this parameter has been selected by comparison with the results of finite element computations carried out for a given set of loading conditions. It was shown that the model still provides accurate results for other loading conditions and configurations.

The results presented in this paper show that inertia may have a significant influence on the development of necking instabilities under dynamic loading and may lead to a substantial increase in ductility. The roles played by strain-rate sensitivity and yield surface shape in dynamic flow localisation are also enlightened. The limit strain predictions appear to be very sensitive to details of the constitutive model, such as the relation used to describe strain-rate sensitivity and the yield surface. This conclusion has already been reported in several studies devoted to quasi-static conditions. However, the situation seems to be more complex when inertia enters into play because of the interaction between inertia effects and the response of the material. This point certainly deserves to be investigated more thoroughly in the future.

Appendix A. Implementation of the two-zone model

This appendix presents the numerical algorithms used for the implementation of the two-zone model. Algorithm 1 is employed for the computation of necking strains for given neck spacing and initial imperfection orientation. Algorithm 2 is used to determine the critical neck spacing and band orientation.

Algorithm 1: computation of necking strains for given neck spacing and initial imperfection orientation

Input data: $\dot{F}_{11}$, $\dot{F}_{22}$, h_0^B, h_0^A, material properties, ψ, L_0, tol (tolerance for the stopping criteria), Δt (time step)

1. Compute $\dot{F}_{\alpha\alpha}$, $\dot{F}_{\alpha\beta}$, $\dot{F}_{\beta\beta}$, $\dot{F}_{\beta\alpha}$ using Eq. (4)

Time integration:

2. Initialisation: $F_{\beta\beta}^A = 1, F_{\alpha\beta}^A = 0, F_{\beta\beta}^B = 1, F_{\alpha\beta}^B = 0,$
$\dot{F}_{\beta\beta}^A = \dot{F}_{\beta\beta}, \dot{F}_{\alpha\beta}^A = \dot{F}_{\alpha\beta}, \dot{F}_{\beta\beta}^B = \dot{F}_{\beta\beta}, \dot{F}_{\alpha\beta}^B = \dot{F}_{\alpha\beta},$
$\bar{\varepsilon}^A = 0, \bar{\varepsilon}^B = 0$
3. Compute strain rates D_{ij}^A and D_{ij}^B using Eq. (25)
4. Compute plastic strain rates $\dot{\bar{\varepsilon}}^A$ and $\dot{\bar{\varepsilon}}^B$ using Eq. (26)
5. Compute Cauchy stresses σ_{ij}^A and σ_{ij}^B using Eqs. (24) and (29)
6. Compute nominal stresses P_{ij}^A and P_{ij}^B using Eqs. (23)
7. Compute Bridgman correction factor $B_1(\phi)$ using Eqs. (32, 35, 36)
8. Compute acceleration gradients $\ddot{F}_{\beta\beta}^A$ and $\ddot{F}_{\alpha\beta}^A$ using Eqs. (22a) and (39)
9. Update velocity and deformation gradients $\dot{F}_{\beta\beta}^A$, $\dot{F}_{\alpha\beta}^A$, $F_{\beta\beta}^A$, $F_{\alpha\beta}^A$:
$$F_{\beta\beta}^A = F_{\beta\beta}^A + \dot{F}_{\beta\beta}^A.\Delta t, \qquad F_{\alpha\beta}^A = F_{\alpha\beta}^A + \dot{F}_{\alpha\beta}^A.\Delta t,$$
$$\dot{F}_{\beta\beta}^A = \dot{F}_{\beta\beta}^A + \ddot{F}_{\beta\beta}^A.\Delta t, \qquad \dot{F}_{\alpha\beta}^A = \dot{F}_{\alpha\beta}^A + \ddot{F}_{\beta\beta}^A.\Delta t$$
10. Compute $\dot{F}_{\beta\beta}^B$, $\dot{F}_{\alpha\beta}^B$, $F_{\beta\beta}^B$, $F_{\alpha\beta}^B$ using Eq. (8)
11. Update effective plastic strains: $\bar{\varepsilon}^A = \bar{\varepsilon}^A + \dot{\bar{\varepsilon}}^A.\Delta t, \qquad \bar{\varepsilon}^B = \bar{\varepsilon}^B + \dot{\bar{\varepsilon}}^B.\Delta t$
12. If $\left(\dot{F}_{\beta\beta}^B/\dot{F}_{\beta\beta}^A > tol\right)$ and $\left(\dot{F}_{\alpha\beta}^B/\dot{F}_{\alpha\beta}^A > tol\right)$, stopping criterion not meet, go to 3
13. Compute the necking strains (principal values of the logarithmic strain tensor in zone B)

Algorithm 2: determination of the critical neck spacing and imperfection orientation

Input data: ψ^{max}, L_o^{max}, L_0^{min}

For ψ in the range $[0, \psi^{max}]$

For L_0 in the range $\left[L_0^{min}, L_o^{max}\right]$

Compute necking strains using Algorithm 1

End for

End for

Search for the set $(\psi\,, L_0)$ leading to the smallest major necking strain

Appendix B. Finite element simulations of plate necking

Numerical simulations of plate necking under biaxial loading were conducted with the finite element software ABAQUS/Explicit. The initial dimensions of the plate are given in Fig. B.1. Most of the simulations were carried out with a mesh that involved 230400 trilinear continuum elements with reduced integration (C3D8R in ABAQUS notation), 120 in direction X_1, 240 in direction X_2 and 8 in direction X_3. To assess the influence of the mesh density, some simulations were also performed using a finer mesh that involved 777600 (180×360×12) elements.

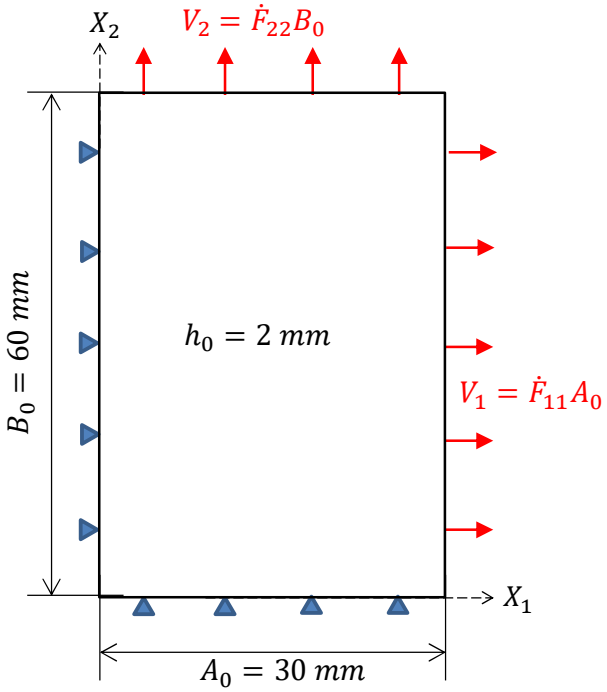

Fig. B.1. Illustration of the configuration considered in the finite element computations of plate necking.

It is well known that imperfections may play a significant role in the development of instabilities under dynamic loading, see for e.g. (Han and Tvergaard, 1995; Sørensen and Freund, 2000; Xue et al., 2008; Vaz-Romero et al., 2017). In the present simulations, random geometric imperfections are considered. They are introduced using the following method: a perfectly regular mesh is first generated and then a small perturbation δX_3 of the position of the nodes in direction X_3 is introduced, with

$$\delta X_3^{(i)} = \eta . \left(\omega^{(i)} - 0.5 \right) \tag{B.1}$$

In this relation, η is the imperfection amplitude, i is the node number and $\omega^{(i)}$ is a random number ranging between 0 and 1. This methodology causes a roughness of the free surfaces of the plate. The root mean squared roughness R_q of the plate free surfaces is linked to the imperfection amplitude by the following relation: $R_q = \eta / \sqrt{12}$. It should be noted that, for a given perturbation amplitude η, it is possible to generate several realisations of the imperfection by changing the seed of the random number generator. In the author's opinion, this kind of imperfection is more representative of defects present in real structures than periodic imperfections. Moreover, with a periodic perturbation, the necking strain is generally dependent on the imperfection wavelength (Xue et al., 2008; Rodríguez-Martínez et al.,

2013a, 2017) and it is necessary to carry out several simulations to identify the critical wavelength and necking strain. A random perturbation involves a wide range of wavelengths and is expected to trigger the most unstable necking mode (because the critical wavelength will be present in the modelling).

The prescribed boundary conditions are

$$V_1(0, X_2, X_3) = 0$$

$$V_1(A_0, X_2, X_3) = \dot{F}_{11} A_0$$

$$V_2(X_1, 0, X_3) = 0$$

$$V_2(X_1, B_0, X_3) = \dot{F}_{22} B_0 \tag{B.2}$$

In order to avoid the generation of stress waves at the beginning of the computations, the following initial velocity field is imposed (the initial velocity field is computed after the introduction of the geometric imperfection).

$$V_1^0 = \dot{F}_{11} X_1$$

$$V_2^0 = \dot{F}_{22} X_2$$

$$V_3^0 = -\left(\dot{F}_{11} + \dot{F}_{22}\right) X_3 \tag{B.3}$$

Table B.1 gives the necking strains derived from the numerical simulations for different imperfection amplitudes. The material has a mass density of 7800 $\mathrm{kg/m^3}$ and an isotopic rate-independent elastic-plastic behaviour obeying the J_2 flow theory. Hardening is described by a power law relation (40) with $n = 0.1$ and $\sigma_0 = 500$ MPa. The loading conditions are $\dot{F}_{22} = 1000\ \mathrm{s^{-1}}$ and $\dot{F}_{11} = 0$ (plane strain tension). With ABAQUS/Explicit, it is not necessary to introduce an imperfection to observe the occurrence of necking, the numerical round-off errors are sufficient to trigger the instability. However, imperfections have a strong influence on the predicted necking strain. Indeed, introducing an imperfection with a small amplitude of $\eta = 1$ µm, the necking strain is reduced by a factor of 2 (compared to the case with no imperfection). For $\eta = 10$ µm, three different random realisations of the imperfection were generated. One can observe that the three realisations lead to almost the same necking strain.

Imperfection amplitude η (µm)	η/h_0 (%)	Realisation #	Necking strain
0	0	-	0.3475
1	0.05	1	0.1769
5	0.25	1	0.1588
10	0.5	1	0.1481
10	0.5	2	0.1454
10	0.5	3	0.1483
20	1	1	0.1364

Table B.1. Influence of the geometric imperfection amplitude on the necking strain derived from the finite element simulations. The necking strain corresponds to the maximum principal value of the logarithmic strain tensor outside the necks at saturation. Rate-independent elastic-plastic behaviour; loading conditions: $\dot{F}_{22} = 1000\ \mathrm{s}^{-1}$, $\dot{F}_{11} = 0$ *(plane-strain deformation).*

Table B.2 illustrates the influence of mesh refinement on the necking strain predictions. With no imperfection ($\eta = 0$), the results are quite sensitive to the mesh size. The necking strain obtained using the fine mesh (M2) is 9% lower than when the coarse mesh (M1) is used. This is not the case when a geometric perturbation is considered, the results obtained with the two meshes being nearly identical.

Imperfection amplitude η (µm)	Realisation #	Necking strain Mesh M1	Necking strain Mesh M2	Difference (%)
0	-	0.3475	0.3188	9
10	1	0.1481	0.1469	
10	2	0.1454	0.1483	
10	3	0.1483	0.1444	
10	Average	0.1473	0.1465	0.5

Table B.2. Necking strains predicted by the finite element simulations for two different meshes (mesh M1: 120×240×8 elements; mesh M2: 180×360×12 elements). The necking strain corresponds to the

maximum principal value of the logarithmic strain tensor outside the necks at saturation. Rate-independent elastic-plastic behaviour; loading conditions: $\dot{F}_{22} = 1000\ \mathrm{s}^{-1}$, $\dot{F}_{11} = 0$ *(plane-strain deformation).*

The numerical results presented in Sections 3.2 and 3.4 have been obtained using the same realisation of an imperfection having an amplitude of $\eta = 10$ µm.

References

Altynova M., Hu X., Daehn G.S., 1996. Increased ductility in high velocity electromagnetic ring expansion. Metallurgical and Materials Transactions A, 27(7), 1837-1844.

Balanethiram V.S., Daehn G.S., 1994. Hyperplasticity: Increased forming limits at high workpiece velocity. Scripta Metallurgica et Materialia, 30(4), 515-520.

Balanethiram V.S., Hu X., Altynova M., Daehn G.S., 1994. Hyperplasticity: enhanced formability at high rates. Journal of Materials Processing Technology, 45(1-4), 595-600.

Banabic D., 2010. Sheet metal forming processes: constitutive modelling and numerical simulation. Springer-Verlag, Berlin Heidelberg.

Banabic D., Barlat F., Cazacu O., Kuwabara T., 2010. Advances in anisotropy and formability. International journal of material forming, 3(3), 165-189.

Barlat F., 1987. Crystallographic texture, anisotropic yield surfaces and forming limits of sheet metals. Materials Science and Engineering, 91, 55-72.

Barlat F., Da Rocha A.B., Jalinier J.M., 1984. Influence of damage on the plastic instability of sheet metals under complex strain paths. Journal of Materials Science, 19(12), 4133-4137.

Boudeau N., Gelin J.C., 2000. Necking in sheet metal forming. Influence of macroscopic and microscopic properties of materials. International journal of mechanical sciences, 42(11), 2209-2232.

Bridgman P.W., 1952. Studies in large plastic flow and fracture, with special emphasis on the effects of hydrostatic pressure. McGRAW-HILL, New-York.

Cazacu O., Revil-Baudard B., 2017. New analytic criterion for porous solids with pressure-insensitive matrix. International Journal of Plasticity, 89, 66-84.

Chu C.C., Needleman A., 1980. Void nucleation effects in biaxially stretched sheets. Journal of engineering materials and technology, 102(3), 249-256.

Chu X., Leotoing L., Guines D., Ragneau E., 2014. Temperature and strain rate influence on AA5086 Forming Limit Curves: Experimental results and discussion on the validity of the MK model. International Journal of Mechanical Sciences, 78, 27-34.

Dequiedt J.L., 2010. Localization in elasto-plastic materials: Influence of the plasticity yield surface in biaxial loading conditions. International Journal of Solids and Structures, 47(21), 2937-2951.

Dequiedt J.L., 2011. Localization in elasto-plastic materials: Influence of an evolving yield surface in biaxial loading conditions. International Journal of Solids and Structures, 48(16-17), 2324-2332.

Dudzinski D., Molinari A., 1988. Instabilité de la déformation viscoplastique en chargement biaxial. Comptes rendus de l'Académie des sciences. Série 2, Mécanique, Physique, Chimie, Sciences de l'univers, Sciences de la Terre, 307(11), 1315-1321.

Dudzinski D., Molinari A., 1991. Perturbation analysis of thermoviscoplastic instabilities in biaxial loading. International Journal of Solids and Structures, 27(5), 601-628.

El Maï S., Mercier S., Petit J., Molinari A., 2014. An extension of the linear stability analysis for the prediction of multiple necking during dynamic extension of round bar. International Journal of Solids and Structures, 51(21-22), 3491-3507.

Ferron G., Mliha Touati M., 1985. Determination of the forming limits in planar-isotropic and temperature-sensitive sheet metals. International Journal of Mechanical Sciences, 27(3), 121-133.

Ferron G., Molinari A., 1989. Mechanical and physical aspects of sheet-metal ductility. Forming Limit Diagrams: Concepts, Methods, and Applications, 111-151, Publisher: The Minerals, Metals & Materials Society.

Fressengeas C., Molinari A., 1994. Fragmentation of rapidly stretching sheets. European journal of mechanics, A/Solids, 13(2), 251-268.

Ghosh A.K., 1977a. Tensile instability and necking in materials with strain hardening and strain-rate hardening. Acta Metallurgica, 25(12), 1413-1424.

Ghosh A.K., 1977b. The influence of strain hardening and strain-rate sensitivity on sheet metal forming. Journal of Engineering Materials and Technology, 99(3), 264-274.

Golovashchenko S.F., Gillard A.J., Mamutov A.V., 2013. Formability of dual phase steels in electrohydraulic forming. Journal of Materials Processing Technology, 213(7), 1191-1212.

Grady D.E., Benson D.A., 1983. Fragmentation of metal rings by electromagnetic loading. Experimental Mechanics, 23(4), 393-400.

Guduru P.R., Freund L.B., 2002. The dynamics of multiple neck formation and fragmentation in high rate extension of ductile materials. International Journal of Solids and Structures, 39(21-22), 5615-5632.

Han J.B., Tvergaard V., 1995. Effect of inertia on the necking behaviour of ring specimens under rapid radial expansion. European journal of mechanics A/Solids, 14(2), 287-307.

Hassannejadasl A., Green D.E., Golovashchenko S.F., Samei J., Maris C., 2014. Numerical modelling of electrohydraulic free-forming and die-forming of DP590 steel. Journal of Manufacturing Processes, 16(3), 391-404.

Hill R., 1952. On discontinuous plastic states, with special reference to localized necking in thin sheets. Journal of the Mechanics and Physics of Solids, 1(1), 19-30.

Hill R., 1987. Constitutive dual potentials in classical plasticity. Journal of the Mechanics and Physics of Solids 35(1), 23-33.

Hosford W.F., 1972. A generalized isotropic yield criterion. Journal of Applied Mechanics, 39(2), 607-609.

Hu X., Daehn G.S., 1996. Effect of velocity on flow localization in tension. Acta Materialia, 44(3), 1021-1033.

Hutchinson J.W., Neale K.W., 1977. Influence of strain-rate sensitivity on necking under uniaxial tension. Acta Metallurgica, 25(8), 839-846.

Hutchinson J.W., Neale K.W., 1978a. Sheet necking-II. Time-independent behavior. In: Mechanics of sheet metal forming, 127-153. Springer, Boston, MA.

Hutchinson J.W., Neale K.W., 1978b. Sheet necking-III. Strain-rate effects. In Mechanics of sheet metal forming (pp. 269-285). Springer, Boston, MA.

Hutchinson J.W., Neale K.W., Needleman A., 1978. Sheet necking—I. Validity of plane stress assumptions of the long-wavelength approximation. In Mechanics of sheet metal forming (pp. 111-126). Springer, Boston, MA.

Jacques N., Mercier S., Molinari A., 2012. Void coalescence in a porous solid under dynamic loading conditions. International journal of fracture, 173(2), 203-213.

Jouve D., 2010. Étude analytique de l'instabilité plastique de striction pour une plaque sollicitée en traction biaxiale. Thèse de Doctorat (Ph. D. Thesis), École Polytechnique et Commissariat à l'Énergie Atomique.

Jouve D., 2015. Analytic study of the onset of plastic necking instabilities during biaxial tension tests on metallic plates. European Journal of Mechanics-A/Solids, 50, 59-69.

Kuroda M., Tvergaard V., 2000. Forming limit diagrams for anisotropic metal sheets with different yield criteria. International Journal of Solids and Structures, 37(37), 5037-5059.

Lee Y.S., Kwon Y.N., Kang S.H., Kim S.W., Lee J.H., 2008. Forming limit of AZ31 alloy sheet and strain rate on warm sheet metal forming. Journal of materials processing technology, 201(1-3), 431-435.

Li M.Y., Zhu X., Chu E., 2012. Effect of strain rate sensitivity on FLDs—an instability approach. International Journal of Mechanical Sciences, 64(1), 273-279.

Lian J., Barlat F., Baudelet B., 1989. Plastic behaviour and stretchability of sheet metals. Part II: Effect of yield surface shape on sheet forming limit. International journal of plasticity, 5(2), 131-147.

Lu Z.H., Lee D., 1987. Prediction of history-dependent forming limits by applying different hardening models. International Journal of Mechanical Sciences, 29(2), 123-137.

Malvern L.E., 1969. Introduction to the Mechanics of a Continuous Medium. Prentice-Hall, Englewood Cliffs, New Jersey.

Marciniak Z., Kuczyński K., 1967. Limit strains in the processes of stretch-forming sheet metal. International journal of mechanical sciences, 9(9), 609-620.

Marciniak Z., Kuczyński K., Pokora T., 1973. Influence of the plastic properties of a material on the forming limit diagram for sheet metal in tension. International Journal of Mechanical Sciences, 15(10), 789-800.

Mercier S., Granier N., Molinari A., Llorca F., Buy F., 2010. Multiple necking during the dynamic expansion of hemispherical metallic shells, from experiments to modelling. Journal of the Mechanics and Physics of Solids, 58(7), 955-982.

Mercier S., Molinari A., 2003. Predictions of bifurcation and instabilities during dynamic extension. International Journal of Solids and Structures, 40(8), 1995-2016.

Molinari A., Jacques N., Mercier S., Leblond J.B., Benzerga A.A., 2015. A micromechanical model for the dynamic behavior of porous media in the void coalescence stage. International Journal of Solids and Structures, 71, 1-18.

Molinari A., Mercier S., Jacques N., 2014. Dynamic failure of ductile materials. Procedia IUTAM, 10, 201-220.

N'souglo K.E., Rodríguez-Martínez J.A., Vaz-Romero A., Cazacu O., 2019. The combined effect of plastic orthotropy and tension-compression asymmetry on the development of necking instabilities in flat tensile specimens subjected to dynamic loading. International Journal of Solids and Structures, 159, 272-288.

Neale K.W., Chater E., 1980. Limit strain predictions for strain-rate sensitive anisotropic sheets. International Journal of Mechanical Sciences, 22(9), 563-574.

Needleman A., Triantafyllidis N., 1978. Void growth and local necking in biaxially stretched sheets. Journal of engineering materials and technology, 100(2), 164-169.

Nie Q.Q., Lee D., 1991. The effect of rate sensitivity on history dependent forming limits of anisotropic sheet metals. Journal of materials shaping technology, 9(4), 233-240.

Parmar A., Mellor P.B., 1978. Predictions of limit strains in sheet metal using a more general yield criterion. International Journal of Mechanical Sciences, 20(6), 385-391.

Rodríguez-Martínez J.A., Molinari A., Zaera R., Vadillo G., Fernández-Sáez J., 2017. The critical neck spacing in ductile plates subjected to dynamic biaxial loading: on the interplay between loading path and inertia effects. International journal of solids and structures, 108, 74-84.

Rodríguez-Martínez J.A., Vadillo G., Fernández-Sáez J., Molinari A., 2013a. Identification of the critical wavelength responsible for the fragmentation of ductile rings expanding at very high strain rates. Journal of the Mechanics and Physics of Solids, 61(6), 1357-1376.

Rodríguez-Martínez J.A., Vadillo G., Zaera R., Fernández-Sáez J., 2013b. On the complete extinction of selected imperfection wavelengths in dynamically expanded ductile rings. Mechanics of Materials, 60, 107-120.

Rohatgi A., Soulami A., Stephens E.V., Davies R.W., Smith M.T., 2014. An investigation of enhanced formability in AA5182-O Al during high-rate free-forming at room-temperature: Quantification of deformation history. Journal of Materials Processing Technology, 214(3), 722-732.

Shenoy V.B., Freund L.B., 1999. Necking bifurcations during high strain rate extension. Journal of the Mechanics and Physics of Solids, 47(11), 2209-2233.

Sørensen N.J., Freund L. B., 2000. Unstable neck formation in a ductile ring subjected to impulsive radial loading. International Journal of Solids and Structures 37(16), 2265-2283.

Stören S., Rice J.R., 1975. Localized necking in thin sheets. Journal of the Mechanics and Physics of Solids, 23(6), 421-441.

Toth L.S., Dudzinski D., Molinari A., 1996. Forming limit predictions with the perturbation method using stress potential functions of polycrystal viscoplasticity. International journal of mechanical sciences, 38(8-9), 805-824.

Tvergaard V., 1978. Effect of kinematic hardening on localized necking in biaxially stretched sheets. International Journal of Mechanical Sciences, 20(9), 651-658.

Vadillo G., Rodríguez-Martínez J.A., Fernández-Sáez J., 2012. On the interplay between strain rate and strain rate sensitivity on flow localization in the dynamic expansion of ductile rings. International journal of solids and structures, 49(3-4), 481-491.

Vaz-Romero A., Rodríguez-Martínez J.A., Mercier S., Molinari A., 2017. Multiple necking pattern in nonlinear elastic bars subjected to dynamic stretching: the role of defects and inertia. International Journal of Solids and Structures, 125, 232-243.

Verleysen P., Peirs J., Van Slycken J., Faes K., Duchene L., 2011. Effect of strain rate on the forming behaviour of sheet metals. Journal of Materials Processing Technology, 211(8), 1457-1464.

Walsh J.M., 1984. Plastic instability and particulation in stretching metal jets. Journal of applied physics, 56(7), 1997-2006.

Xue Z., Vaziri A., Hutchinson J.W., 2008. Material aspects of dynamic neck retardation. Journal of the Mechanics and Physics of Solids 56(1), 93-113.

Zaera R., Rodríguez-Martínez J.A., Vadillo G., Fernández-Sáez J., Molinari A., 2015. Collective behaviour and spacing of necks in ductile plates subjected to dynamic biaxial loading. Journal of the Mechanics and Physics of Solids 85, 245-269.

Zhang H., Ravi-Chandar K., 2006. On the dynamics of necking and fragmentation–I. Real-time and post-mortem observations in Al 6061-O. International Journal of Fracture, 142(3-4), 183-217.

Zhang H., Ravi-Chandar K., 2008. On the dynamics of necking and fragmentation—II. Effect of material properties, geometrical constraints and absolute size. International Journal of Fracture, 150(1-2), 3-36.

Zhang H., Ravi-Chandar K., 2010. On the dynamics of localization and fragmentation-IV. Expansion of Al 6061-O tubes. International Journal of Fracture, 163(1-2), 41-65.

Zhou F., Molinari J.F., Ramesh K.T., 2006. An elastic–visco-plastic analysis of ductile expanding ring. International journal of impact engineering, 33(1-12), 880-891.